1 **POMINO-GEMS: A Research Product for Tropospheric NO₂ Columns from**

2 **Geostationary Environment Monitoring Spectrometer**

3 Yuhang Zhang[1], Jintai Lin[1], Jhoon Kim[2], Hanlim Lee[3], Junsung Park[3], Hyunkee Hong[4], Michel Van

4 Roozendael[5], Francois Hendrick[5], Ting Wang[6,7], Pucai Wang[6,7], Qin He[8], Kai Qin[8], Yongjoo Choi[9],

5 Yugo Kanaya[10], Jin Xu[11], Pinhua Xie[7,11], Xin Tian[12], Sanbao Zhang[13], Shanshan Wang[13], Siyang

6 Cheng[14], Xinghong Cheng[14], Jianzhong Ma[14], Thomas Wagner[15], Robert Spurr[16], Lulu Chen[17], Hao

7 Kong[1], Mengyao Liu[18]

8 [1]Laboratory for Climate and Ocean-Atmosphere Studies, Department of Atmospheric and Oceanic

9 Sciences, School of Physics, Peking University, Beijing, 100871, China

10 [2]Department of Atmospheric Sciences, Yonsei University, Seoul, South Korea

11 [3]Pukyong National University, Busan, South Korea

12 [4]National Institute of Environmental Research, Incheon, South Korea

13 [5]Belgian Institute for Space Aeronomy (BIRA-IASB), Brussels, Belgium

14 [6]CNRC & LAGEO, Institute of Atmospheric Physics, Chinese Academy of Sciences, Beijing, 100029,

15 China

16 [7]University of Chinese Academy of Sciences, Beijing, 100049, China

17 [8]School of Environment and Geoinformatics, China University of Mining and Technology, Xuzhou,

18 Jiangsu, 221116, China

19 [9]Department of Environmental Science, Hankuk University of Foreign Studies, Yongin, South Korea

20 [10]Research Institute for Global Change, Japan Agency for Marine-Earth Science and Technology

21 (JAMSTEC), Yokohama, 2360001, Japan

22 [11]Key Laboratory of Environmental Optics and Technology, Anhui Institute of Optics and Fine

23 Mechanics, Chinese Academy of Science, Hefei, 230031, China

24 [12]Information Materials and Intelligent Sensing Laboratory of Anhui Province, Institutes of Physical

25 Science and Information Technology, Anhui University, Hefei, Anhui, 230601, China

26 [13]Shanghai Key Laboratory of Atmospheric Particle Pollution and Prevention (LAP3), Department of

27 Environmental Science and Engineering, Fudan University, Shanghai, 200433, China

28 [14]State Key Laboratory of Severe Weather & Institute of Tibetan Plateau Meteorology, Chinese Academy

29 of Meteorological Sciences, Beijing, 100081, China

30 [15]Max Planck Institute for Chemistry, 55020, Mainz, Germany

31 [16]RT Solutions Inc., Cambridge, Massachusetts, 02138, USA

32 [17]College of Urban and Environmental Sciences, Peking University, Beijing, 100871, China

33 [18]R&D Satellite Observations Department, Royal Netherlands Meteorological Institute, De Bilt, the

34 Netherlands

35 *Correspondence to*: Jintai Lin (linjt@pku.edu.cn)

36 **Abstract**

37 Tropospheric vertical column densities (VCDs) of nitrogen dioxide (NO₂) retrieved from sun-

38 synchronous satellite instruments have provided abundant NO₂ data for environmental studies, but such

39   data are limited by retrieval uncertainties and insufficient temporal sampling (e.g., once a day). The

40   Geostationary Environment Monitoring Spectrometer (GEMS) launched in February 2020 monitors NO_2

41   at an unprecedented hourly resolution during the daytime. Here we present a research product for

42   tropospheric NO_2 VCDs, referred to as POMINO-GEMS. We develop a hybrid retrieval method

43   combining GEMS, TROPOMI and GEOS-CF data to generate hourly tropospheric NO_2 slant column

44   densities (SCDs). We then derive tropospheric NO_2 air mass factors (AMFs) with explicit corrections for

45   surface reflectance anisotropy and aerosol optical effects, through parallelized pixel-by-pixel radiative

46   transfer calculations. Prerequisite cloud parameters are retrieved with the O_2-O_2 algorithm by using

47   ancillary parameters consistent with those used in NO_2 AMF calculations.

48   Initial retrieval of POMINO-GEMS tropospheric NO_2 VCDs for June–August 2021 exhibits strong

49   hotspot signals over megacities and distinctive diurnal variations over polluted and clean areas.

50   POMINO-GEMS NO_2 VCDs agree with the POMINO-TROPOMI v1.2.2 product ($R = 0.98$, and NMB

51     $= 4.9\%$) over East Asia, with slight differences associated with satellite viewing geometries and cloud

52   and aerosol properties affecting the NO_2 retrieval. POMINO-GEMS also shows good agreement with

53   OMNO2 v4 ($R = 0.87$, and NMB $= -16.8\%$) and GOME-2 GDP 4.8 ($R = 0.83$, and NMB $= -1.5\%$) NO_2

54   products. POMINO-GEMS shows small biases against ground-based MAX-DOAS NO_2 VCD data at

55   nine sites (NMB $= -11.1\%$) with modest or high correlation in diurnal variation at six urban and suburban

56   sites (R from 0.60 to 0.96). The spatiotemporal variation of POMINO-GEMS correlates well with

57   mobile-car MAX-DOAS measurements in the Three Rivers' Source region on the Tibetan Plateau ($R =$

58   0.81). Surface NO_2 concentrations estimated from POMINO-GEMS VCDs are consistent with

59   measurements from the Ministry of Ecology and Environment of China for spatiotemporal variation (R

60     $= 0.78$, and NMB $= -26.3\%$) as well as diurnal variation at all, urban, suburban and rural sites ($R \geq 0.96$).

61   POMINO-GEMS data will be made freely available for users to study the spatiotemporal variations,

62   sources and impacts of NO_2.

63   **1. Introduction**

64   Tropospheric nitrogen dioxide (NO_2) is an important air pollutant. It threats human health, and

65   contributes to the formation of tropospheric ozone (O_3) and nitrate aerosols (Crutzen, 1970; Shindell et

66   al., 2009; Hoek et al., 2013; Chen et al., 2022). Satellite instruments provide observations of tropospheric

67   NO_2 on a global scale, and they have been extensively used to estimate emissions of nitrogen oxides

68   (NO_x = NO + NO_2) (Lin and Mcelroy, 2011; Beirle et al., 2011; Gu et al., 2014; Kong et al., 2022a),

69   surface NO_2 concentrations (Wei et al., 2022; Cooper et al., 2022), trends and variabilities (Richter et al.,

70   2005; Cui et al., 2016; Krotkov et al., 2016; Van Der A et al., 2017), and impacts on human health and

71   environment (Chen et al., 2021).

72   To date, most spaceborne instruments for NO_2 measurements, including the Global Ozone

73   Monitoring Instrument (GOME) (Burrows, 1999), the Ozone Monitoring Instrument (OMI) (Levelt et

74   al., 2006), the Global Ozone Monitoring Experiment 2 (GOME-2) (Callies et al., 2000) and the

75   TROPOspheric Monitoring Instrument (TROPOMI) (Veefkind et al., 2012), are mounted on sun-

76   synchronous low Earth orbit (LEO) satellites. These instruments passively measure backscattered

77   radiance from the Earth's atmosphere, and measurements at each ground location are done 1–2 times a

78   day. The Geostationary Environment Monitoring Spectrometer (GEMS) on board the Geostationary

79   Korea Multi-Purpose Satellite-2B (GK-2B) was successfully launched in February 2020. The instrument

80   provides measurements of NO_2 and other pollutants in the daytime on an hourly basis (Kim et al., 2020).

81   It complements LEO satellite observations by providing a more comprehensive picture of the daytime

82   evolution of NO_2.

83   There are three successive stages in the retrieval of tropospheric NO_2 vertical column densities

84   (VCDs) in the UV-Vis range based on satellite observations. The first step is to retrieve total NO_2 slant

85   column densities (SCDs) with spectral fitting techniques, such as the Differential Optical Absorption

86   Spectroscopy (DOAS). The SCD represents the abundance of NO_2 along the effective light path from

87   the sun through the atmosphere to the satellite instrument. Next, the contributions from stratospheric NO_2

88   to the total SCDs are removed in order to obtain tropospheric SCDs. Finally, the tropospheric SCDs are

89   converted to VCDs using calculated air mass factors (AMFs). The AMF calculations are highly sensitive

90   to the observation geometry, cloud parameters, aerosols, surface conditions and the shape of the NO_2

91   vertical distribution. Over polluted areas, errors in the retrieved tropospheric NO_2 VCDs are dominated

92   by the uncertainties in AMF calculations (Boersma et al., 2004; Lorente et al., 2016) associated with

93   aerosol optical effects, surface reflectance and a priori NO_2 vertical profiles (Zhou et al., 2010; Lin et al.,

94   2014; Lin et al., 2015; Vasilkov et al., 2016; Lorente et al., 2018; Liu et al., 2019; Liu et al., 2020;

95   Vasilkov et al., 2021).

96   The official GEMS retrieval algorithm for tropospheric NO_2 VCDs is developed by Lee et al. (2020).

The total NO_2 SCDs are retrieved using the DOAS technique. They are then converted to total NO_2 VCDs by using a precomputed look-up table of box AMFs based on the linearized pseudo-spherical scalar and vector discrete ordinate radiative transfer code (VLIDORT) version 2.6. Finally, stratosphere-troposphere separation (STS) is performed to derive tropospheric NO_2. Validation results have shown the overall capability of the official GEMS NO_2 algorithm (Kim et al., 2023), but several problems are also reported, such as overestimation of total NO_2 SCDs and tropospheric NO_2 VCDs, and some degree of striping in NO_2 retrieval data.

In this study, we present a research product which we name as POMINO-GEMS. This product is built upon our Peking University OMI NO_2 (POMINO) algorithm which focuses on the tropospheric AMF calculations and has been applied to OMI and TROPOMI (Lin et al., 2014; Lin et al., 2015; Liu et al., 2019; Liu et al., 2020; Zhang et al., 2022). Here we extend the AMF calculation by constructing a hybrid method to estimate tropospheric SCDs for GEMS. The hybrid method makes use of the total SCDs from the official GEMS product, total SCDs and stratospheric VCDs from the official TROPOMI product, as well as hourly stratospheric VCD data from the NASA Global Earth Observing System Composition Forecast (GEOS-CF) v1 product. We validate our initial set of retrieval results for tropospheric NO_2 VCDs in June-July-August (JJA) 2021, by using independent data of tropospheric NO_2 from the POMINO-TROPOMI v1.2.2, OMNO2 v4 and GOME-2 GDP 4.8 products, ground-based and mobile-car MAX-DOAS measurements, and surface concentration observations from the Ministry of Ecology and Environment (MEE) of China. We provide a simplified estimate of retrieval errors in the end.

2. Method and data

2.1 Construction of POMINO-GEMS retrieval algorithm

Figure 1 shows the flow chart of POMINO-GEMS retrieval algorithm. There are two essential steps. The first is to calculate tropospheric NO_2 SCDs on an hourly basis, through fusion of total SCDs from the official GEMS v1.0 L2 NO_2 product, total SCDs and stratospheric VCDs from the TROPOMI PAL v2.3.1 L2 NO_2 product, and diurnal variations of stratospheric NO_2 from the GEOS-CF v1 product. We then calculate tropospheric NO_2 AMFs to convert SCDs to VCDs.
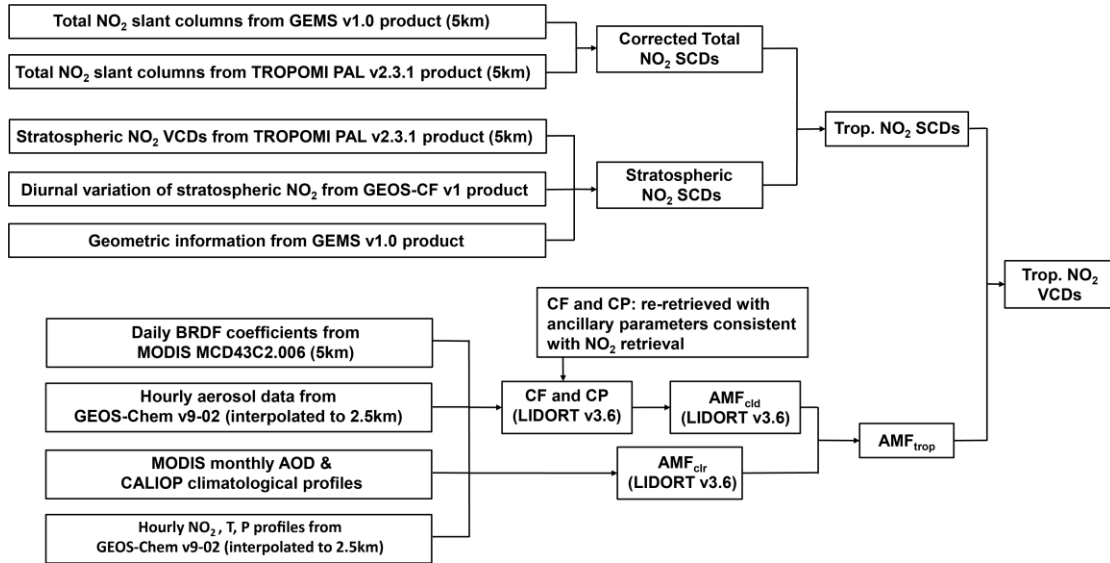
Total NO$_2$ slant columns from GEMS v1.0 product (5km)

Total NO$_2$ slant columns from TROPOMI PAL v2.3.1 product (5km)

Corrected Total NO$_2$ SCDs

Stratospheric NO$_2$ VCDs from TROPOMI PAL v2.3.1 product (5km)

Diurnal variation of stratospheric NO$_2$ from GEOS-CF v1 product

Geometric information from GEMS v1.0 product

Stratospheric NO$_2$ SCDs

Trop. NO$_2$ SCDs

Trop. NO$_2$ VCDs

Daily BRDF coefficients from MODIS MCD43C2.006 (5km)

Hourly aerosol data from GEOS-Chem v9-02 (interpolated to 2.5km)

MODIS monthly AOD & CALIOP climatological profiles

Hourly NO$_2$, T, P profiles from GEOS-Chem v9-02 (interpolated to 2.5km)

CF and CP: re-retrieved with ancillary parameters consistent with NO$_2$ retrieval

CF and CP (LIDORT v3.6)

AMF$_{cld}$ (LIDORT v3.6)

AMF$_{clr}$ (LIDORT v3.6)

AMF$_{trop}$

Figure 1. Flow chart of POMINO-GEMS retrieval algorithm. The numbers in the boxes, such as 5 km, refer to horizontal resolutions.

2.1.1 GEMS NO$_2$ and cloud data

The GEMS instrument is on board the GK-2B satellite locating at 128.2°E over the equator (Kim et al., 2020). The spectral wavelength range of GEMS is 300-500 nm, covering main absorption spectra of aerosols and trace gases. The nominal spatial resolution is typically 7 km × 8 km for gases and 3.5 km × 8 km for aerosols in the eastern and central scan domains; however, the north-south spatial resolution can exceed 25 km in the western side. The whole field of view (FOV) covers about 20 Asian countries within latitudes 5°S to 45°N and longitudes 80°E to 152°E. Given the variation of solar zenith angle (SZA), there are four scan scenarios moving from east to west, including Half East (HE), Half Korea (HK), Full Central (FC) and Full West (FW). It takes 30 minutes (for example, 00:45 – 01:15 UTC) for GEMS to scan its full coverage during each scenario, and the next 30 minutes to transmit data to the ground data center. The number of hourly GEMS observations per day varies from 6 in winter to 10 in summer, corresponding to the annual movement of subsolar points relative to the Earth.

We take hourly total (stratospheric + tropospheric) NO$_2$ SCDs from the official GEMS v1.0 L2 NO$_2$ product, and convert them to 0.05° × 0.05 ° gridded data by means of an area-weighted oversampling technique. The value of each grid cell is the mean value of pixel-based GEMS observations weighted by the ratio of the overlap area of each pixel to the area of grid cell. We also use continuum reflectance data (i.e., spectrally smooth reflectance from molecular and aerosol extinction as well as surface reflectance effects) and O$_2$-O$_2$ SCDs from the official GEMS v1.0 L2 cloud product to re-calculate cloud parameters

145 as a prerequisite for tropospheric NO$_2$ AMF calculations. Details of the GEMS retrievals can be found

146 in the algorithm theoretical basis document (ATBD) (Lee et al., 2020).

2.1.2 TROPOMI, OMI and GOME-2 NO$_2$ data

148 Table S1 compares the basic information of GEMS with those of TROPOMI, OMI and GOME-2

149 instruments. In this study, TROPOMI data are used for derivation of POMINO-GEMS NO$_2$ VCDs, and

150 data from all of the three LEO instruments are used for comparison with POMINO-GEMS.

151 We use total NO$_2$ SCDs and stratospheric NO$_2$ VCDs from the official TROPOMI PAL v2.3.1 L2

152 NO$_2$ product, and convert them to 0.05° × 0.05 °gridded data, again using an area-weighted oversampling

153 technique. Details of TROPOMI total SCD retrievals and stratospheric VCD calculations are given in

154 the TROPOMI ATBD (Van Geffen et al., 2022a). The TROPOMI PAL product is reprocessed with

155 TROPOMI NO$_2$ data processor v2.3.1 for the period from 1 May 2018 to 14 November 2021; it will be

156 replaced by the full mission reprocessing with NO$_2$ processor v2.4.0 in the future (Eskes et al., 2021).

157 The most important improvement in this PAL product upon the previous OFFL v1.3 is the replacement

158 of the FRESCO-S algorithm with the FRESCO-wide cloud retrieval algorithm, which leads to higher,

159 more reasonable cloud pressure (CP) estimates and substantial increases in tropospheric NO$_2$ VCDs (by

160 20% – 50%) over polluted regions like Eastern China in winter (Eskes et al., 2021; Van Geffen et al.,

161 2022b).

162 We use the POMINO-TROPOMI v1.2.2, OMNO2 v4 (Krotkov et al., 2019) and GOME-2 GDP 4.8

163 (Valks et al., 2019) tropospheric NO$_2$ VCD products to compare with POMINO-GEMS results. The

164 previous POMINO-TROPOMI v1 data show higher accuracy in polluted situations and improved

165 consistency with MAX-DOAS measurements when compared with the official TM5-MP-DOMINO

166 (OFFLINE) product (Liu et al., 2020). POMINO-TROPOMI v1.2.2 improves upon v1 by (1) using

167 tropospheric NO$_2$ SCD and CP data from the updated TROPOMI PAL v2.3.1 NO$_2$ product, (2)

168 interpolating the daily NO$_2$, pressure, temperature and aerosol vertical profiles from nested GEOS-Chem

169 (v9-02) simulations into a horizontal grid of 2.5 km x 2.5 km for subsequent tropospheric AMF

170 calculations, and (3) including several minor bug fixes.

171 We select valid satellite pixels following common practice. For the daily POMINO-TROPOMI

172 v1.2.2 L2 NO$_2$ product, we exclude pixels with SZA or viewing zenith angle (VZA) greater than 80°,

173 high albedos caused by ice or snow on the ground, quality flag values (from the TROPOMI PAL v2.3.1

174   product) less than 0.5 or cloud radiance fraction (CRF) greater than 50%, and then map the valid data to

175   a 0.05° × 0.05 ° grid. For the daily OMNO2 v4 L2 NO_2 product, we exclude pixels with SZA or VZA

176   greater than 80°, with scene Lambert-equivalent reflectivity (LER) greater than 0.3, affected by row

177   anomaly (XTrackQualityFlags is not zero), marked without quality assurance (vcdQualityFlag is not an

178   even integer) or with CRF greater than 50%, and then map the valid data to a 0.25° × 0.25 ° grid. For the

179   daily GOME-2 GDP 4.8 L2 NO_2 product, we exclude pixels with latitude greater than 70°, SZA greater

180   than 80°, failed retrieval (NO2Tropo_Flag is set to 1 or 2) or with CRF greater than 50%, and then map

181   the valid data to a 0.5° × 0.5° grid.

182   **2.1.3 GEOS-CF stratospheric NO_2 data**

183   The NASA GEOS-CF system combines the Global Earth Observing System (GEOS) weather

184   analysis and forecasting system with GEOS-Chem v12.0.1 chemistry module (http://geoschem.org) to

185   provide near real-time estimates of atmospheric compositions with daily 5-day forecasts. Detailed

186   information of the model, including chemistry, emissions and deposition, and evaluation of the GEOS-

187   CF tropospheric simulation and forecast skill are presented in Keller et al. (2021). In particular, the

188   GEOS-Chem v12.0.1 chemistry scheme includes online stratospheric chemistry that is fully coupled with

189   tropospheric chemistry through the Unified tropospheric-stratospheric Chemistry eXtension (UCX)

190   mechanism (Eastham et al., 2014). The GEOS-CF stratospheric results are consistent with satellite

191   observations, albeit with notable underestimation of NO_x and HNO_3 in the polar regions (Knowland et

192   al., 2022b).

193   The GEOS-CF outputs have a horizontal resolution of 0.25° × 0.25 ° and a temporal resolution of 1

194   hour for NO_2 and other ancillary data used here (Knowland et al., 2022a). We convert instantaneous

195   stratospheric NO_2 volume mixing ratio in dry air at each hour (e.g., 00:00 UTC) into 0.05° × 0.05 °

196   gridded vertical column densities based on estimated tropopause information in GEOS-CF v1. In Section

197   2.1.5, we first evaluate GEOS-CF v1 stratospheric NO_2 VCDs with those of TROPOMI PAL v2.3.1

198   product, and then calculate hourly stratospheric NO_2 VCDs by combining GEOS-CF v1 data for each

199   hour and TROPOMI PAL v2.3.1 stratospheric NO_2 VCD data in the early afternoon.

200   **2.1.4 Calculation of total NO_2 SCDs**

201   We use TROPOMI data to correct GEMS total NO_2 SCDs, given known issues in GEMS data.

202   Specifics for the NO_2 SCD retrieval of TROPOMI PAL v2.3.1 and GEMS v1.0 operational products are

7

203   provided in Table S2.

204   Figure 2a and b show the spatial distribution of monthly mean total NO_2 geometric column densities

205   (GCDs, calculated as SCDs divided by geometric AMFs) in June 2021 from TROPOMI PAL v2.3.1 and

206   GEMS v1.0, respectively. The horizontal resolution is $0.05° \times 0.05°$. The GCDs are used to compare the

207   two products after removing the effect of measurement geometry. Matching for each day between hourly

208   GEMS observations and the TROPOMI data at the closest observation time is done to ensure temporal

209   compatibility. The figures show that the spatial pattern of GEMS GCDs agrees well with that of

210   TROPOMI, with high values over the North China Plain (NCP) and Northwestern India, as well as major

211   metropolitan clusters such as Seoul and the Yangtze River Delta (YRD). However, there are two

212   systematic problems in GEMS GCDs. First, the GEMS GCD values are abnormally high over the

213   northern and northwestern parts of GEMS FOV, especially over Mongolia, Qinghai, Inner Mongolia,

214   Xinjiang and Tibet of China. Second, west-east stripes exist over the whole domain, similar to the

215   spurious across-track variability issue for OMI. This stripe issue exists at all hours (Figure S1). It is likely

216   associated with the specific scan modes of GEMS, as well as periodically occurring bad pixels as one of

217   remaining calibration issues (Boersma et al., 2011; Lee et al., 2023).
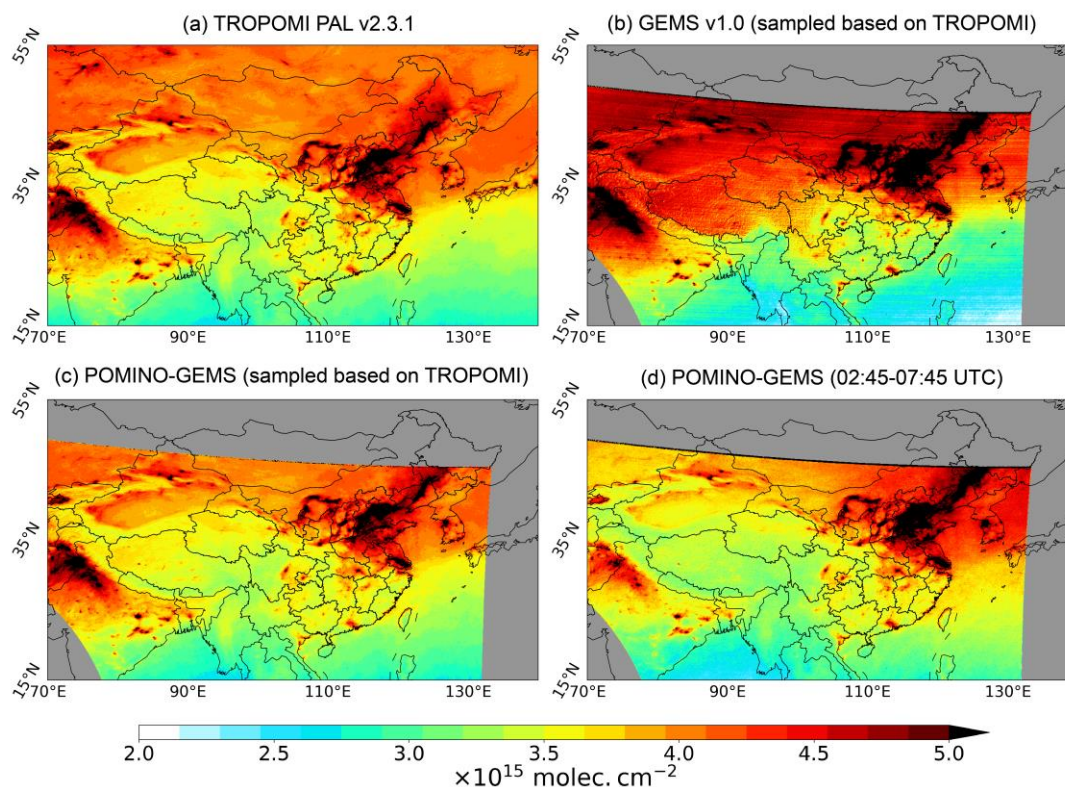
Figure 2. Spatial distribution of monthly mean total NO_2 GCDs on a $0.05° \times 0.05°$ grid in June 2021. (a) The
TROPOMI PAL v2.3.1 product, (b) the official GEMS v1.0 product that spatiotemporally matches with
TROPOMI, (c) the corrected POMINO-GEMS product that spatiotemporally matches with TROPOMI,

224 To correct the two issues in the GEMS official total NO_2 SCD product, we combine GEMS and

225 TROPOMI observations to obtain hourly $0.05° \times 0.05°$ corrected total NO_2 SCDs for each day using Eqs.

226 (1) and (2):

$$\Delta GCD = \frac{1}{n} \sum_{i=1}^{n} (GCD_{total,h_i}^{TROPOMI} - GCD_{total,h_i}^{GEMS}) \tag{1}$$

$$SCD_{total,h}^{corrected} = SCD_{total,h}^{GEMS} + \Delta GCD \times AMFgeo_h^{GEMS} \tag{2}$$

229 In Eqs. (1) and (2), index h represents the hour of GEMS observations on each day; h_i the hour

230 when both GEMS and TROPOMI have valid observations for the same grid cell; and n the number of h_i.

231 The value of n is 1 or 2 depending on the overpass times of TROPOMI. There are two steps in the

232 correction process. First, we calculate a geometry-independent correction map for each day using total

233 NO_2 GCDs from GEMS and TROPOMI that match spatially and temporally (Eq. (1)). We use the

234 absolute difference instead of a scaling factor as a simple correction. We then apply the correction to the

235 original GEMS total NO_2 SCDs at each hour on the same day, with the diurnal variation in AMF

236 associated with measurement geometry accounted for (Eq. (2)).

237 In Eq. (2), we implement a simple geometric correction (concerning SZAs and VZAs) for AMFs

238 instead of using the actual AMFs; the latter could account for the differences in relative azimuth angles

239 and other factors. Specific derivation of this assumption is given in Section 1 of the Supplement

240 Information (SI). The correction is assumed to be acceptable with an extra uncertainty introduced to the

241 total NO_2 SCDs, as will be further discussed in Section 3.5.

242 Figure 2c shows the monthly mean corrected POMINO-GEMS total NO_2 GCDs in June 2021 after

243 spatial and temporal matching with TROPOMI. The corrected GCD values in the northern GEMS FOV

244 are much reduced compared with those in the original GEMS data. Moreover, most stripe-like patterns

245 are removed in the corrected GCDs. Figure 2d is similar to Fig. 2c but for GCDs averaged over 02:45 –

246 07:45 UTC in June 2021. Figure S3 further compares the original GEMS and POMINO-GEMS total

247 NO_2 GCDs at each hour in JJA 2021, showing similar improvements as well. The differences between

248 Figure 2c and d indicate the influence of different sampling hours combined with the daily correction

249 map. Specifically, the correction value of each grid cell is calculated at the specific hour when both

250 GEMS and TROPOMI have valid observations, but this value is applied to original GEMS SCDs at all

251   hours.

252   Our correction method is done for each grid cell. We tested other correction methods by applying

253   the same correction value to grid cells within a $20° \times 20°$ domain, at the same latitude, or at the same

254   longitude. These alternative methods can reduce the high bias over the northern and northwestern GEMS

255   FOV to various extents, but cannot remove the stripes (not shown). We also note that our simple

256   correction is a temporary solution before the aforementioned systematic problems in the official GEMS

257   SCD retrieval are solved by improving spectral fitting. In Sections 3.3 and 3.4, we compare the diurnal

258   variations of tropospheric NO_2 VCDs based on corrected and uncorrected GEMS SCDs.

259   2.1.5 Calculation of stratospheric and tropospheric NO_2 SCDs

260   We construct a dataset of hourly stratospheric NO_2 SCDs at $0.05° \times 0.05°$ by using TROPOMI PAL

261   v2.3.1 stratospheric NO_2 VCDs, diurnal variation of stratospheric NO_2 VCDs provided by GEOS-CF v1

262   product, and GEMS geometric AMFs.

263   Figure S4 shows the comparison results between GEOS-CF v1 and TROPOMI PAL v2.3.1

264   stratospheric NO_2 VCDs in June 2021. Consistent spatial and temporal sampling is done. N is the total

265   number of matched $0.05° \times 0.05°$ grid cells. The stratospheric VCDs from both products vary in the range

266   of $2 - 5 \times 10^{15}$ molec. cm^{-2}, with spatiotemporal correlation of 0.99, linear regression slope of 0.99 and

267   normalized mean bias (NMB) of 0.02%. This consistency provides confidence on the overall reliability

268   of GEOS-CF stratospheric NO_2 data.

269   First, we calculate stratospheric NO_2 VCDs at a reference hour for each day using Eqs. (3) and (4):

270     $$\text{ratio}_{h_0}^h = \frac{\text{VCD}_{\text{strat},h}^{\text{GEOS-CF}}}{\text{VCD}_{\text{strat},h_0}^{\text{GEOS-CF}}} \tag{3}$$

271     $$\text{VCD}_{\text{strat},h_0} = \frac{1}{n} \sum_{i=1}^{n} \frac{\text{VCD}_{\text{strat},h_i}^{\text{TROPOMI}}}{\text{ratio}_{h_0}^{h_i}} \tag{4}$$

272   Here, Eq. (3) defines the ratio of GEOS-CF stratospheric NO_2 at hour h to that at the reference hour

273   h_0, which is chosen to be 01:00 UTC (Figure S5). In Eq. (4), h_i represents the observation time of every

274   TROPOMI orbit that overlaps with GEMS FOV, and n the number of h_i for each grid cell.

275   Second, we use the ratio from a given time h to h_0 and stratospheric NO_2 VCDs at h_0 to derive

276   stratospheric NO_2 VCDs at h for each day (Eq. (5)).

277     $$\text{VCD}_{\text{strat},h} = \text{VCD}_{\text{strat},h_0} \times \text{ratio}_{h_0}^h \tag{5}$$
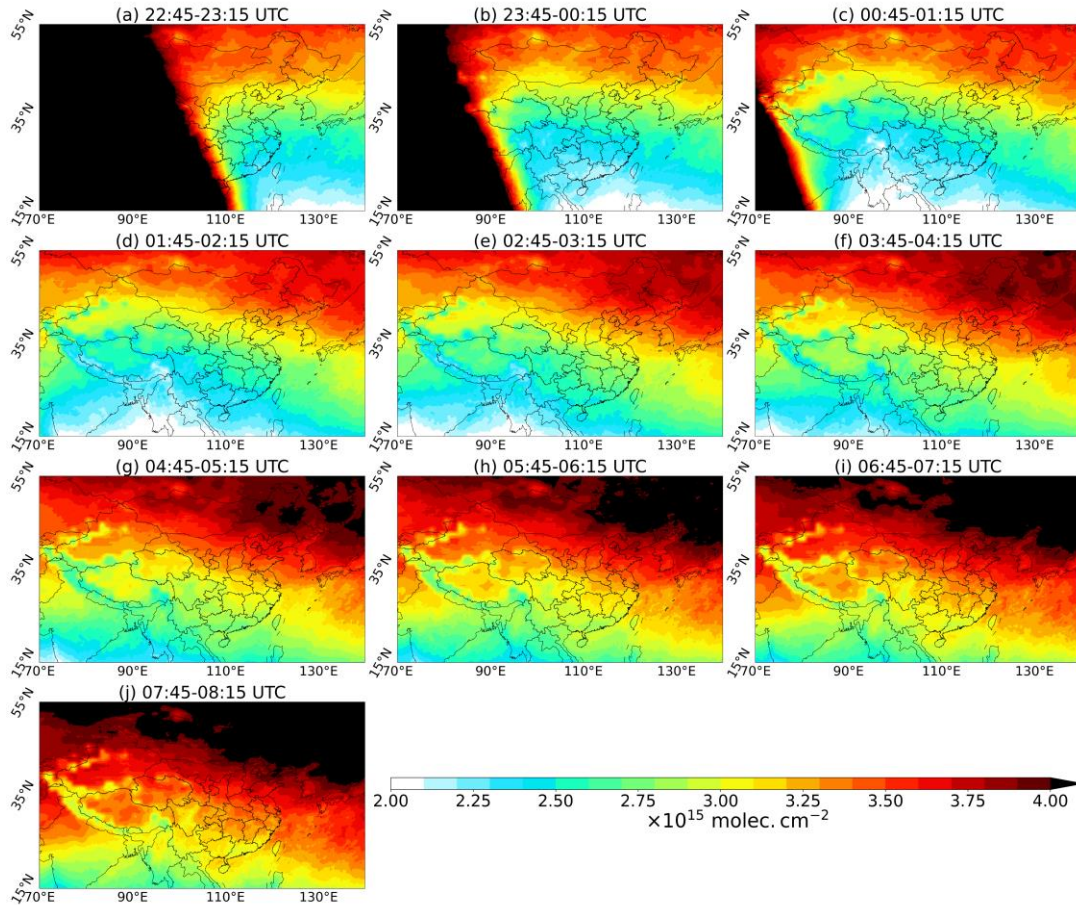
278   Figure 3 shows the derived monthly mean stratospheric NO_2 VCDs at each hour in June 2021 on a

279   0.05° × 0.05 ° grid. The abrupt decease of stratospheric NO_2 VCDs after sunrise is caused by resumed

280   photochemical conversion of NO_2 to NO (Li et al., 2021b). There is a strong meridional gradient of

281   stratospheric NO_2 in the daytime, with the higher values in the north associated with longer lifetimes.

282   The stratospheric NO_2 increase quasi-linearly during the daytime; linear regression to the mean

283   stratospheric NO_2 VCDs over the whole domain from 01:45 to 07:45 UTC results in an increasing rate

284   of $(1.12\pm0.03) \times 10^{14}$ molec. cm^{-2} h^{-1}. This result is consistent with previous work showing quasi-linear

285   growth in the daytime at rates of $0.5 - 2 \times 10^{14}$ molec. cm^{-2} h^{-1} depending on latitude and season (Li et

286   al., 2021b; Dirksen et al., 2011).

287   Finally, we use GEMS geometric AMFs to convert the stratospheric NO_2 VCDs to SCDs at each

288   hour, and then subtract them from the total SCDs to obtain tropospheric SCDs (Eqs. (6) and (7)). In the

289   stratosphere, the geometric AMFs are essentially the same as the actual AMFs

290    $$SCD_{strat,h} = VCD_{strat,h} \times AMFgeo_h^{GEMS} \qquad (6)$$

291    $$SCD_{trop,h}^{GEMS*} = SCD_{total,h}^{corrected} - SCD_{strat,h} \qquad (7)$$

292

293   **Figure 3. Spatial distribution of POMINO-GEMS derived monthly mean stratospheric NO_2 VCDs at each**

294   **hour on a 0.05° × 0.05 ° grid in June 2021. Note the range of the color bar is $2.0 - 4.0 \times 10^{15}$ molec. cm^{-2}.**

2.1.6 Calculation of tropospheric AMFs

Tropospheric NO_2 AMF is dependent on three factors as defined in Palmer et al. (2001): the viewing geometry, the scattering weights describing the sensitivity of the backscattered spectrum to the abundance of the absorber, and a priori NO_2 vertical profile (Eq. (8)).

$$\text{AMF} = \text{AMF}_G \int_0^{z_T} w(z)S(z)\text{d}z \qquad (8)$$

In Eq. (8), AMF_G is the geometric AMF and a function of SZA and VZA, $w(z)$ the scattering weight at altitude z, $S(z)$ the normalized vertical profile of NO_2 number density, and z_T the tropopause. Following Yang et al. (2023), we refer to $\int_0^{z_T} w(z)S(z)\text{d}z$ as the scattering correction factor for discussion in Section 3.2. For tropospheric AMF calculations (Figure 1), we use a parallelized AMFv6 package driven by LIDORT version 3.6; this is similar to the one used in our previous POMINO products (Lin et al., 2014; Lin et al., 2015; Liu et al., 2019) but with modifications to adapt to the geostationary observing characteristics and high spatiotemporal resolution of GEMS. We take daily BRDF coefficients with a horizontal resolution of 5 km from the MODIS MCD43C2.006 dataset (Lucht et al., 2000) to account for the anisotropy of surface reflectance over land and coastal ocean regions , and OMLER v3 albedo over open ocean (Zhou et al., 2010; Lin et al., 2014; Liu et al., 2020). Hourly-varying aerosol parameters, a priori NO_2 profiles, temperature profiles and pressure profiles are interpolated from nested GEOS-Chem (v9-02) results to a horizontal resolution of 2.5 km, using the Piecewise Cubic Hermite Interpolating Polynomial (PCHIP) method. Furthermore, we deploy AOD observations from the MODIS/Aqua Collection 6.1 MYD04_L2 dataset to constrain model-simulated AOD on a monthly basis (Lin et al., 2014; Lin et al., 2015; Liu et al., 2019; Liu et al., 2020); and we use a self-constructed monthly climatological dataset of aerosol extinction profiles based on CALIOP L2 data over 2007-2015 to constrain modeled aerosol vertical profiles on a monthly climatology basis (Liu et al., 2019). We re-retrieve cloud parameters based on O_2-O_2 SCDs and continuum reflectances from the official GEMS v1.0 cloud product, using ancillary parameters consistent with those used in NO_2 AMF calculations. Instead of relying on a look-up table (LUT), we conduct pixel-by-pixel radiative transfer calculations with the parallelized AMFv6 package. The independent pixel approximation (IPA) is assumed for cloud-contaminated pixels as in other algorithms. Finally, we use the AMF data to convert tropospheric NO_2 SCDs to VCDs.

Invalid pixels in the POMINO-GEMS product are filtered based on the following criteria. We

12

324 exclude pixels with SZA or VZA greater than 80°, or with the ground covered by ice or snow. To

325 minimize cloud contamination, we exclude pixels with CRF greater than 50%.

326 **2.2 Estimation of surface NO₂ concentrations**

327 In order to validate satellite NO₂ products with surface concentration measurements from MEE, we

328 convert tropospheric NO₂ VCDs from satellite products on a 0.05° × 0.05° grid to surface NO₂ mass

329 concentrations using GEOS-Chem simulated NO₂ vertical profiles and the box heights of the lowest

330 model layer (Eq. (9)).

331
$$C_{\text{surf}} = \text{VCD}_{\text{trop}}^{\text{SAT}} \times R^{\text{GC}} \times \frac{M}{N \times H^{\text{GC}}} \times 2 \tag{9}$$

332 In Eq. (9), C_{surf} represents the estimated surface NO₂ mass concentration in μg m⁻³, $\text{VCD}_{\text{trop}}^{\text{SAT}}$ the

333 satellite tropospheric VCD in molecules. m⁻², R^{GC} the GEOS-Chem simulated hourly ratio of NO₂ sub-

334 column in the lowest layer to the total tropospheric column, M the NO₂ molar mass in μg mol⁻¹, N the

335 Avogadro constant, and H^{GC} the box height of the lowest layer in m. The thickness of the lowest layer

336 of GEOS-Chem (about 130 m) is too large for the layer average NO₂ mass concentration to represent

337 that near the ground (Liu et al., 2018a); thus the derived concentration is multiplied by a factor of 2 to

338 roughly account for the vertical gradient from the height of ground instrument to the center of the model

339 layer. However, the constant correction factor of 2 neglects the diurnal variation of NO₂ vertical gradient,

340 which is related to the diurnal variation of planetary boundary layer (PBL) heights. This issue is discussed

341 in detail in Section 3.4.

342 **2.3 Ground-based MAX-DOAS measurements**

343 We use ground-based MAX-DOAS NO₂ measurements, together with POMINO-TROPOMI v1.2.2,

344 OMNO2 v4 and GOME-2 GDP 4.8 NO₂ products, to validate the POMINO-GEMS retrieval results. The

345 types, geolocations and observation times of MAX-DOAS stations are summarized in Table S3, and the

346 location of each site is shown in Figure S6. Details of each site are described in Section 2 of the SI.

347 Kanaya et al. (2014) and Hendrick et al. (2014) have discussed the error in MAX-DOAS NO₂ retrieval:

348 uncertainties from a priori aerosol and NO₂ profiles are the largest source by 10% – 14%, and the total

349 retrieval uncertainty is typically 12% – 17%.

350 To ensure sampling consistency in time, we average all valid MAX-DOAS measurements within

351 each observation period of GEMS (i.e., 30 minutes) for hourly comparison, and within ± 1.5 h of

TROPOMI, OMI and GOME-2 overpass time for daily comparison. Following the procedures in previous studies (Lin et al., 2014; Liu et al., 2020), we exclude all matched MAX-DOAS data for which the standard deviation exceeds 20% of the mean value to minimize the influence of local events. To ensure sampling consistency in space, we select valid satellite pixels within 5 km of MAX-DOAS sites for POMINO-GEMS and POMINO-TROPOMI v1.2.2, 25 km for OMNO2 v4 and 50 km for GOME-2 GDP 4.8, and conduct spatial averaging. The Grubbs statistical test, which is used to detect outliers in a univariate data set assumed to exhibit normal distribution (Grubbs, 1950), is performed to exclude outliers in both MAX-DOAS and satellite data before comparison. Only one data pair from Fudan University site is identified as an outlier and removed (Figure S7), and we get 1348 matched hourly data pairs in total.

2.4 Mobile-car MAX-DOAS measurements

We use tropospheric NO_2 VCDs from mobile-car MAX-DOAS measurements performed by the Chinese Academy of Meteorological Sciences (CAMS) in the Three Rivers' Source region in July 2021 (Cheng et al., 2023). The Three Rivers' Source region is on the northeastern Tibetan Plateau in western China, which is isolated from massive anthropogenic activities, and hence a good place for observations of atmospheric compositions in the background atmosphere. The field campaign lasted from 18th to 30th July 2021 and included four closed-loop journeys, beginning from the meteorological bureau of the city of Xining (the Capital of Qinghai Province) to the meteorological bureau of Dari County of the Guoluo Tibetan Autonomous Prefecture, to the meteorological bureau of Yushu Tibetan Autonomous Prefecture, and then back to Xining City (Figure S6). The spectral analysis of the measurement spectra in the fitting window of 400-434 nm was implemented with the DOAS method. Sequential Fraunhofer reference spectrum (FRS) is used to derive NO_2 differential slant column densities (DSCDs), which are then converted to VCDs by adopting the geometric approximation method. The errors are estimated to be less than 20% at high altitudes. More detailed descriptions of instrumentation, field campaign and data retrieval are in Cheng et al. (2023).

We average all valid mobile-car MAX-DOAS measurements within each observation period of GEMS in each $0.05° \times 0.05°$ grid cell, to ensure spatiotemporal consistency. Over relatively clean areas with little human influence and biomass burning such as the Three Rivers' Source region, a large portion of NO_2 is located in the middle and upper troposphere, which is not accounted for in the mobile-car data

14

381 via such a DSCD-based retrieval method. Indeed, Cheng et al. (2023) showed that the official TROPOMI

382 NO$_2$ VCDs are higher than mobile-car data by about 40%. Considering that the diurnal variation of

383 middle and upper tropospheric NO$_2$ is much smaller than that in the lower troposphere, we focus on the

384 correlation of NO$_2$ diurnal variation between POMINO-GEMS and mobile car MAX-DOAS data.

2.5 Ground-based MEE NO$_2$ measurements

386 We use hourly surface NO$_2$ mass concentration measurements from the MEE air quality monitoring

387 network. By 2021, more than 2000 MEE stations across China have been established, providing hourly

388 observations for NO$_2$ and five other air pollutants. Most stations are in urban or suburban areas.

389 The spatial distribution of all MEE sites in the GEMS FOV is shown in Figure S8a, and that of MEE

390 sites over urban, suburban and rural regions are shown in Figure S8b–d, respectively. The classification

391 of sites is based on Tencent user location data with a horizontal resolution of 0.05° × 0.05 °for every 0.5

392 second from 31 August to 30 September 2021 (Figure S8e), adopted from previous work (Kong et al.,

393 2022a). Here, urban MEE sites are defined as where the mean location request times is larger than 50

394 times per second, suburban sites refer to 5-50 times per second, and rural sites refer to less than 5 times

395 per second. The number of sites for urban, suburban and rural sites are 808, 554 and 71, respectively.

396 At MEE sites, molybdenum catalyzed conversion from NO$_2$ to NO and subsequent

397 chemiluminescence measurement of NO is done to estimate NO$_2$ concentrations. The heated

398 molybdenum catalyst has low chemical selectivity, leading to strong interference from other oxidized

399 nitrogen species such as nitric acid (HNO$_3$) and peroxyacetyl nitrate (PAN). Therefore, MEE data tend

400 to overestimate the actual NO$_2$ concentrations, with the extent of overestimation about 10% – 50%

401 (Boersma et al., 2009; Liu et al., 2018a). The overestimation is dependent on the oxidation level of NO$_x$,

402 but is currently unclear for each site and hour.

403 To compare with satellite-derived surface NO$_2$ concentration data, we average over all valid MEE

404 sites in each 0.05° × 0.05 °grid cell to generate gridded MEE NO$_2$ data for each hour. To ensure sampling

405 consistency for each day, we average MEE observations at two consecutive hours to match GEMS hourly

406 observations – for example, we match the mean value of MEE NO$_2$ concentrations in 13:00 – 14:00 and

407 14:00 – 15:00 local solar time (LST) with the GEMS NO$_2$ in 13:45 – 14:15 LST. We also match MEE

408 observations over the period 13:00 – 14:00 LST with TROPOMI-derived and OMI-derived surface NO$_2$,

409 and 9:00 – 10:00 LST with GOME-2-derived surface NO$_2$.

## 3. Results and discussion

3.1 POMINO-GEMS tropospheric NO₂ VCDs

Figure 4 shows mean POMINO-GEMS tropospheric NO_2 VCDs at each hour on a 0.05° × 0.05° grid in JJA 2021. High values of tropospheric NO_2 columns ($> 10 \times 10^{15}$ molec. cm⁻²) are evident over populous regions such as South Korea, central and eastern China, and northern India. Clear hotspot signals reveal intense NO_x emissions over city clusters such as Beijing-Tianjin-Hebei (BTH), Yangtze River Delta (YRD), Pearl River Delta (PRD) and Seoul Metropolitan Area (SMA), as well as isolated megacities such as Osaka and Nagoya in Japan, Chengdu and Urumqi in China, and New Delhi in India. Tropospheric NO_2 VCDs are much lower ($< 1 \times 10^{15}$ molec. cm⁻²) over most of western China and the open ocean, due to low anthropogenic and natural emissions.
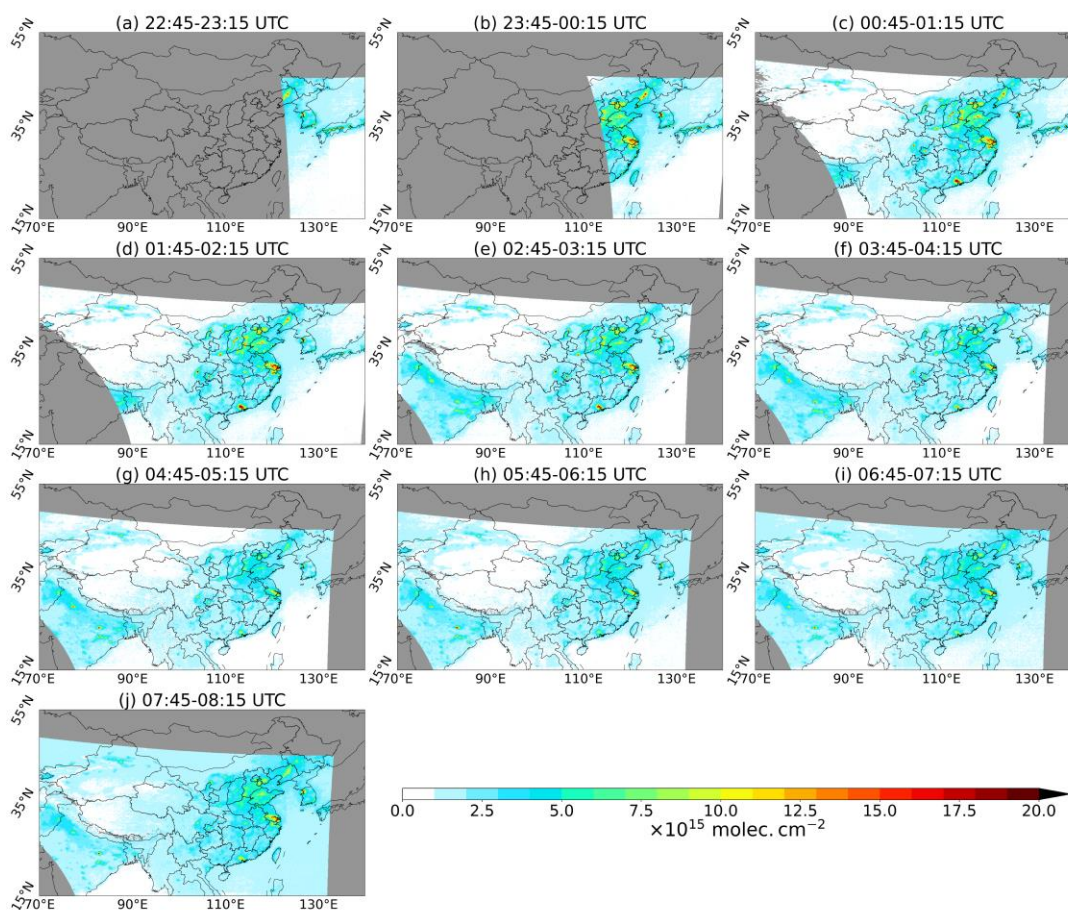
Figure 4. Spatial distribution of POMINO-GEMS tropospheric NO₂ VCDs at each hour on a 0.05° × 0.05° grid in JJA 2021. The regions in grey mean there are no valid observations.

Figure 5a-c present NO_2 VCDs in the morning, noon and afternoon in JJA 2021 for eastern China. Data are averaged in 22:45 – 01:45 UTC (06:45 – 09:45 Beijing Time, BJT), 02:45 – 04:45 UTC (10:45

425 – 12:45 BJT) and 05:45 – 07:45 UTC (13:45 – 15:45 BJT) to represent the morning, noon and afternoon,

426 respectively. In the morning (Figure 5a), there are clear city signals with high NO_2 values, reflecting

427 abundant NO_x emissions from traffic. The spatial gradients of NO_2 from urban centers to outskirts are

428 very strong. However, these spatial gradients are greatly reduced in the noon and afternoon (Figure 5b

429 and c). For example, the differences of tropospheric NO_2 VCDs between the urban center of Xi'an

430 (108.93°N, 34.27°E) and its surrounding areas (within 50 km) are reduced from about 8×10^{15} molec.

431 cm^{-2} in the morning to about 4×10^{15} molec. cm^{-2} at noon, and then to below 2×10^{15} molec. cm^{-2} in the

432 afternoon. This is likely due to chemical loss of traffic-associated NO_2, increased emissions from other

433 sectors (e.g., industry), and/or enhanced horizontal transport smearing the spatial gradient.
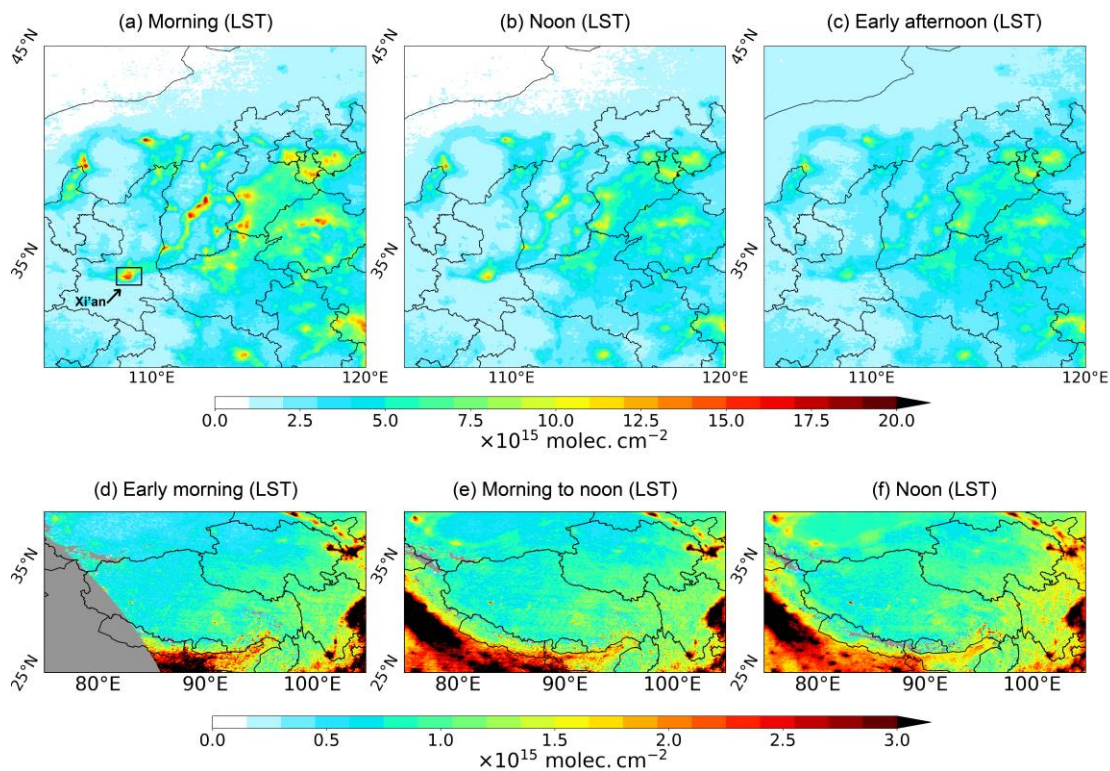
434
435 **Figure 5. Spatial distribution of three-hour-mean POMINO-GEMS tropospheric NO₂ VCDs in JJA 2021 on**
436 **a 0.05° × 0.05 ° grid. The first row is for eastern China in the (a) morning (22:45 – 01:45 UTC), (b) noon**
437 **(02:45 – 04:45 UTC) and (c) afternoon (05:45 – 07:45 UTC). The second row is for western China in the (d)**
438 **early morning (00:45 – 01:45 UTC), (e) morning to noon (02:45 – 04:45 UTC) and (f) noon (05:45 – 07:45**
439 **UTC). The regions in grey mean there are no valid observations.**

440 Over western China with low tropospheric NO_2 VCDs (Figure 5d-f), there is a gradual increase of

441 tropospheric NO_2 by about 1×10^{15} molec. cm^{-2} from the early morning to noon. This increase is likely

442 dominated by biogenic NO_x emissions that are sensitive to sunshine intensity and surface temperature

443 (Kong et al., 2022b; Weng et al., 2020; Kong et al., 2023). Future studies are needed to understand the

17

444   exact causes.

445   Figure 6 shows the diurnal variation of POMINO-GEMS tropospheric NO_2 VCDs over six different

446   region groups in the GEMS FOV. The six groups are defined based on the levels of mean POMINO-

447   GEMS tropospheric NO_2 VCDs at 12:00 LST in JJA 2021 ($VCD_{12:00\ LST}$), and their spatial distributions

448   are also shown in each panel. We convert the observation time from UTC to LST for each time zone in

449   this domain (+5 time zone: 70°E – 82.5° E; +6 time zone: 82.5°E – 97.5°E; +7 time zone: 97.5°E –

450   112.5°E; +8 time zone: 112.5°E – 127.5°E; +9 time zone: 127.5°E – 140°E), and show the NO_2 diurnal

451   variations in each time zone with different colors. For low NO_2 situations ($VCD_{12:00\ LST} \leq 2 \times 10^{15}$ molec.

452   cm^{-2}), NO_2 grow in the morning time in +5 and +6 time zones but not in other time zones. Over high

453   NO_2 situations ($VCD_{12:00\ LST} > 8 \times 10^{15}$ molec. cm^{-2}, in cities and suburban areas), NO_2 in all time zones

454   exhibit a minimum around noontime and a morning peak at 09:00 – 10:00 LST, consistent with previous

455   findings for specific polluted locations (Boersma et al., 2008; Boersma et al., 2009; Li et al., 2021a;

456   Ghude et al., 2020; Herman et al., 2019; Biswas and Mahajan, 2021). In all groups and time zones,

457   tropospheric NO_2 VCDs grow from noon to the afternoon.

458   The NO_2 diurnal variations are related to multiple driving factors. Different sources with distinctive

459   diurnal patterns dominate the NO_x emissions over different regions. Lightning and biogenic activities are

460   the major emission sources over low NO_2 land areas, and they tend to intensify with temperature and

461   radiation in the daytime. Anthropogenic emissions are dominant over polluted cities and suburban areas,

462   where the traffic emissions tend to peak in the mid-morning and late afternoon (Jing et al., 2016; Liu et

463   al., 2018b; Naiudomthum et al., 2022). In addition, the photochemistry plays an important role. NO_2 is

464   in chemical balance with NO, and the ratio of NO_2 and NO depends on radiation, ozone and peroxyl

465   radicals. NO_x is oxidized to nitric acid and organic nitrates by radicals in the daytime, the level of which

466   depends on radiation, ozone and volatile organic compounds. Thus the lifetime of NO_2 reaches the

467   minimum value around noon, i.e., a few hours in summer. Furthermore, atmospheric transport also affects

468   the diurnal variation of NO_2 at high-value places (e.g., cities) and their surroundings. Further studies are

469   needed to determine the exact causes of NO_2 diurnal variations at individual places.
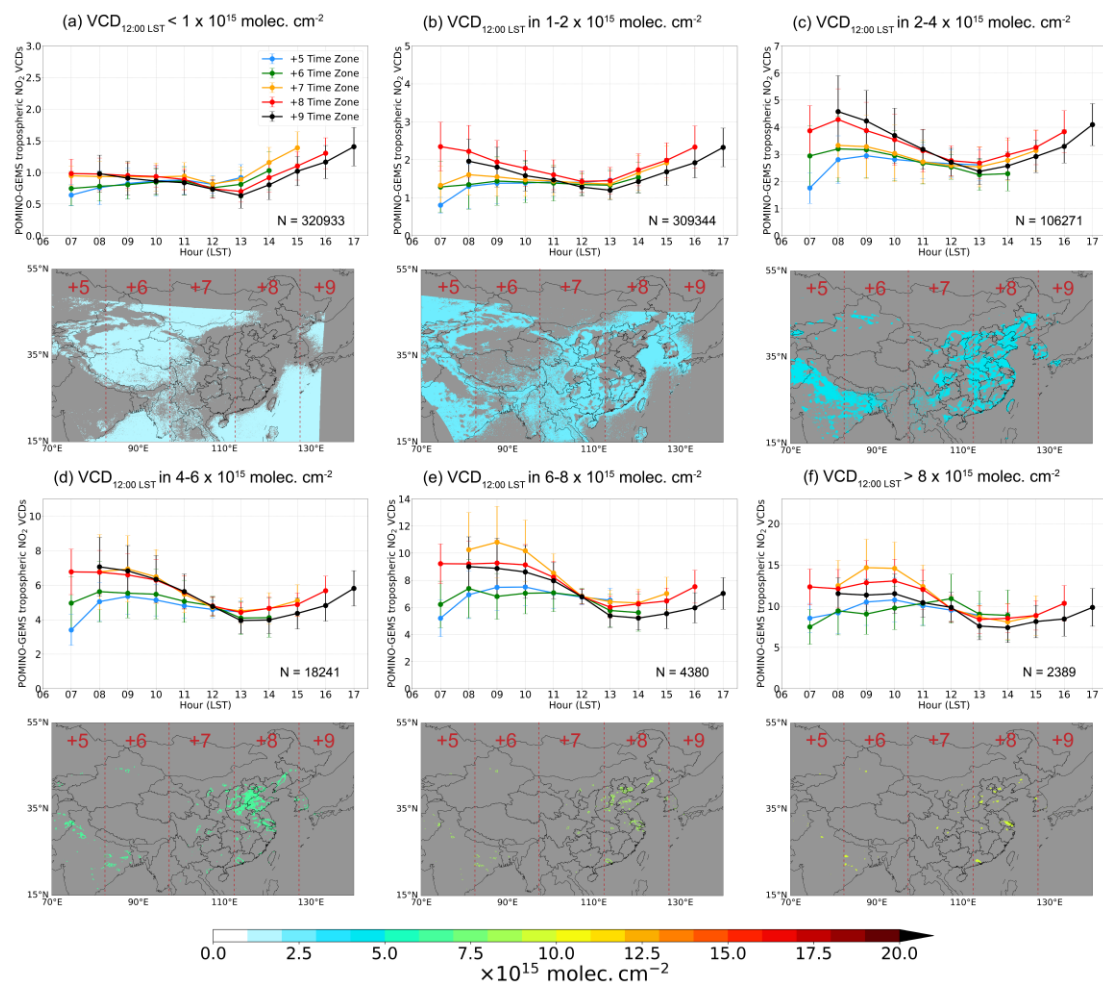
Figure 6. POMINO-GEMS NO₂ diurnal variations for six region groups classified based on mean POMINO-GEMS tropospheric NO₂ VCDs at 12:00 LST in JJA 2021 (VCD$_{12:00 LST}$). (a) VCD$_{12:00 LST}$ less than 1×10^{15} molec. cm⁻²; (b) VCD$_{12:00 LST}$ in $1 - 2 \times 10^{15}$ molec. cm⁻²; (c) VCD$_{12:00 LST}$ in $2 - 4 \times 10^{15}$ molec. cm⁻²; (d) VCD$_{12:00 LST}$ in $4 - 6 \times 10^{15}$ molec. cm⁻²; (e) VCD$_{12:00 LST}$ in $6 - 8 \times 10^{15}$ molec. cm⁻² and (f) VCD$_{12:00 LST}$ larger than 8×10^{15} molec. cm⁻². In each panel, different colors denote the NO₂ diurnal variation in different time zones. N denotes the total number of valid $0.05° \times 0.05°$ grid cells in each region. The error bars denote the standard deviation of tropospheric NO₂ VCDs at each hour in each time zone.

3.2 Comparison with POMINO-TROPOMI v1.2.2, OMNO2 v4 and GOME-2 GDP 4.8 NO₂ VCD products

Figure 7a and b show the POMINO-GEMS and POMINO-TROPOMI v1.2.2 tropospheric NO₂ VCDs, respectively, on a $0.05° \times 0.05°$ grid averaged over JJA 2021. Cloud screening is implemented based on the CRFs from each product. To ensure temporal compatibility, matching between hourly GEMS observations and the TROPOMI data at the closest observation time is done for each day. Overall, POMINO-GEMS agrees well with POMINO-TROPOMI with a spatial correlation coefficient of 0.98, a linear regression slope of 1.18 and a small positive NMB of 4.9% (Figure 7c). Regionally, POMINO-

486 GEMS VCDs are higher than those of POMINO-TROPOMI v1.2.2 over eastern China, most India and

487 northwestern GEMS FOV, but smaller over western China and the oceans (Figure 7a, b; see Figure S9c

488 and d for differences plots). These differences are related to tropospheric NO_2 AMFs and SCDs. Detailed

489 discussion is given in Section 3 of the SI.

490
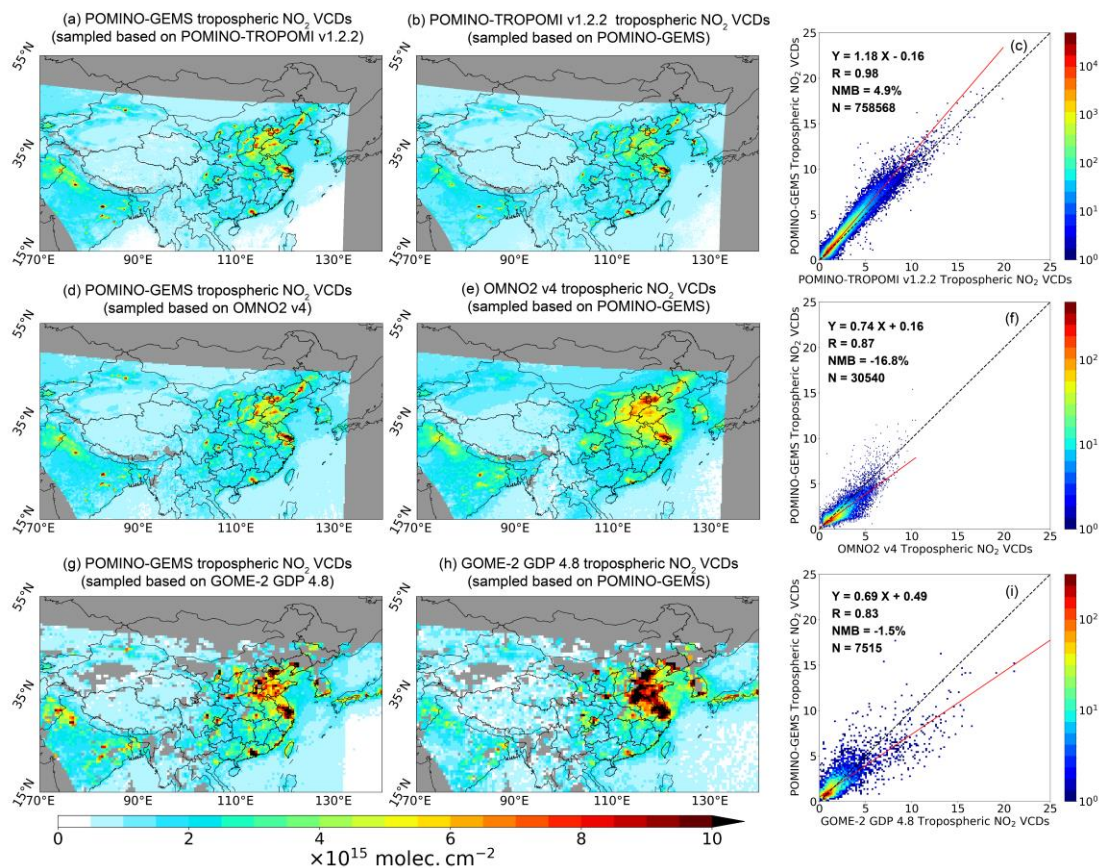
Figure 7. Comparison between POMINO-GEMS and other products for tropospheric NO₂ VCDs in JJA

2021. (a-b) Between POMINO-GEMS and POMINO-TROPOMI v1.2.2 on a 0.05° × 0.05 °grid, (d-e)

between POMINO-GEMS and OMNO2 v4 on a 0.25° × 0.25 °grid, and (g-h) between POMINO-GEMS and

GOME-2 GDP 4.8 on a 0.5° × 0.5 °grid. (c), (f) and (i) are respective scatterplots, in which the colors

represent data density. The regions in grey mean there are no valid observations.

496 Figure 7d-f and g-i show the comparison results of POMINO-GEMS tropospheric NO_2 VCDs with

497 OMNO2 v4 on a 0.25° × 0.25° grid and GOME-2 GDP 4.8 on a 0.5° × 0.5 °grid averaged over JJA 2021,

498 respectively. POMINO-GEMS NO_2 VCDs exhibit good spatial consistency with the two independent

499 products (R = 0.87 and 0.83), although with slightly lower values than OMNO2 v4 (by 16.8%) and

500 GOME-2 GDP 4.8 (by 1.5%). These VCD differences are expected, considering the differences in the

501 retrieval algorithm. For example, the POMINO-GEMS algorithm implements explicit aerosol

502 corrections in the radiative transfer calculation, while OMNO2 v4 and GOME-2 GDP 4.8 treat aerosols

503 as "effective clouds". POMINO-GEMS accounts for the anisotropy of surface reflectance by adopting

504 MODIS BRDF coefficients, whereas OMNO2 v4 and GOME-2 GDP 4.8 use geometry-dependent and

505 regular LER, respectively. The horizontal resolution of a priori NO_2 profiles in POMINO-GEMS is 25

506 km (and interpolated to 2.5 km), $1° \times 1.25°$ in OMNO2 v4 and $1.875° \times 1.875°$ in GOME-2 GDP 4.8

507 (Krotkov et al., 2019; Valks, 2019).

508   Based on comparisons with POMINO-TROPOMI v1.2.2, OMNO2 v4 and GOME-2 GDP 4.8 NO_2

509 VCDs, we conclude that POMINO-GEMS NO_2 columns show good agreement with LEO satellite data,

510 with lower values by 20% at most.

3.3 Validation with MAX-DOAS NO_2 VCD measurements

512   The scatterplot in Figure 8a compares POMINO-GEMS tropospheric NO_2 VCDs in JJA 2021 at all

513 GEMS observation hours with matched ground based MAX-DOAS measurements at nine sites.

514 POMINO-GEMS correlates with MAX-DOAS ($R = 0.66$) with a small negative bias (NMB = −11.1%).

515 The linear regression shows a slope of 0.51 and intercept of 3.34×10^{15} molec. cm^{-2}, reflecting

516 underestimation of POMINO-GEMS tropospheric NO_2 VCDs on high-NO_2 days.
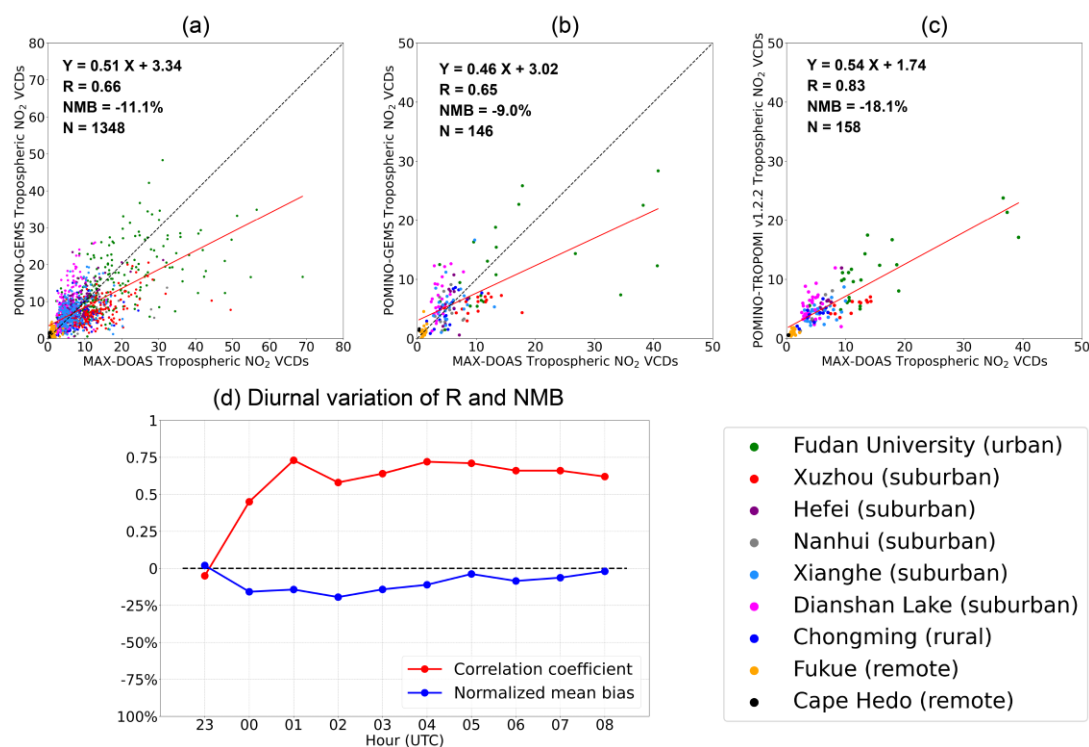
Figure 8. Evaluation of satellite NO_2 VCD data using ground-based MAX-DOAS measurements. (a)

Scatterplot for tropospheric NO_2 VCDs ($\times 10^{15}$ molec. cm^{-2}) between MAX-DOAS and POMINO-GEMS at

all GEMS observation hours in JJA 2021. Each data pair denotes an hour. (b-c) Scatterplots for

tropospheric NO_2 VCDs ($\times 10^{15}$ molec. cm^{-2}) in JJA 2021 (b) between MAX-DOAS and POMINO-GEMS at

13:45 – 14:15 LST and (c) between MAX-DOAS and POMINO-TROPOMI v1.2.2. Each data pair denotes a

day. Each MAX-DOAS station is color-coded. (d) Diurnal variations of spatiotemporal correlation

524   **coefficients and NMBs of POMINO-GEMS tropospheric NO$_2$ VCDs relative to ground-based MAX-DOAS**

525   **data.**

526   Figure 8b-c further use MAX-DOAS measurements to evaluate POMINO-GEMS and POMINO-

527   TROPOMI v1.2.2 tropospheric NO$_2$ VCDs at the overpass time of TROPOMI. In Figure 8b, POMINO-

528   GEMS data at 13:45 – 14:15 LST are used to match the overpass time of TROPOMI. The POMINO-

529   TROPOMI product is evaluated in the context of understanding the relative performance of POMINO-

530   GEMS. Each data point represents a day. Figure 8b-c show that the day-to-day variability of MAX-

531   DOAS measurements is well captured by POMINO-TROPOMI v1.2.2 (R = 0.83), but less so by

532   POMINO-GEMS (R = 0.65). Linear regression results show an underestimate of tropospheric NO$_2$ VCDs

533   in POMINO-TROPOMI v1.2.2 (NMB = −18.1%), as also found in previous studies (Liu et al., 2020).

534   POMINO-GEMS exhibits a small bias (NMB = −9.0%), but station-dependent performance is apparent.

535   At the two remote sites of Fukue and Cape Hedo with low NO$_2$, POMINO-GEMS NO$_2$ columns are

536   higher than those of MAX-DOAS measurements. At the other sites, the data pairs are more scattered and

537   located both above and below the 1:1 line, resulting in a small NMB.

538   Figure 8d shows the NMBs and correlation coefficients of POMINO-GEMS NO$_2$ VCDs relative to

539   ground-based MAX-DOAS data at each hour. The NMBs are negative at most hours except 23:00 UTC

540   (07:00 BJT). The negative NMBs reach a maximum of about 20% at 02:00 UTC (10:00 BJT), and

541   decrease to less than 10% in the afternoon. The correlation coefficients are modest or high (0.45 – 0.73)

542   at most hours, with the exception at the first hour which is likely due to few valid data (N = 17).

543   Figure 9 compares the diurnal variation of tropospheric NO$_2$ VCDs between POMINO-GEMS and

544   MAX-DOAS at eight stations. At each site, NO$_2$ values are averaged in JJA 2021 at each hour for

545   comparison, and the number of valid days for each hour is also shown. The Cape Hedo site is not included

546   because there are few valid MAX-DOAS data points at each hour. Figure 10a-f show that at the urban

547   and suburban sites, MAX-DOAS NO$_2$ (black lines) peaks in the mid-to-late morning, declines towards

548   the minimum values at noon around 13:00 LST, and then gradually increases in the afternoon. Strong

549   correlation of NO$_2$ diurnal variation between POMINO-GEMS (red solid lines) and MAX-DOAS is

550   found at Xuzhou (R = 0.82), Hefei (R = 0.96), Fudan University (R = 0.84), Nanhui (R = 0.79) and

551   Xianghe (R = 0.94). At the Dianshan Lake site, POMINO-GEMS NO$_2$ columns increase but MAX-

552   DOAS data decrease from 08:00 to 09:00 LST, resulting in a lower correlation coefficient (R = 0.60). At

553   Chongming and Fukue sites, MAX-DOAS NO$_2$ shows a peak in the morning without evident increase in

22

the early afternoon, but this diurnal pattern is not fully captured by POMINO-GEMS. At Fukue,

POMINO-GEMS NO$_2$ exhibit abrupt changes at 12:00 and 13:00 LST due to few valid data.

In addition, comparison of POMINO-GEMS diurnal variation with NO$_2$ data from GOME-2 in the

morning and OMI and TROPOMI in the early afternoon shows good agreement at Hefei, Nanhui,

Dianshan Lake, Chongming and Fukue sites. The differences between POMINO-GEMS to MAX-DOAS

NO$_2$ VCDs are comparable or smaller than those between LEO satellite and MAX-DOAS NO$_2$ VCDs.
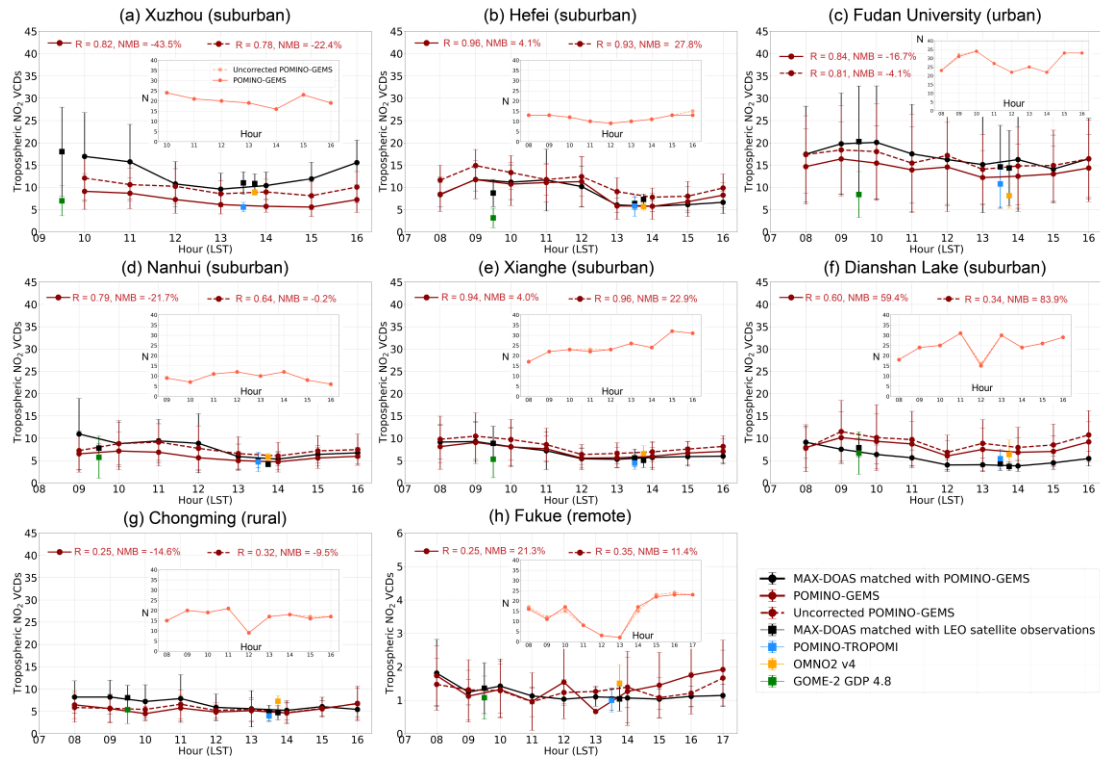
Figure 9. Diurnal variation of hourly tropospheric NO$_2$ VCDs (× 10^{15} molec. cm^{-2}) of MAX-DOAS (black lines), and POMINO-GEMS with TROPOMI correction (red solid lines). and re-calculated POMINO-GEMS without TROPOMI correction (red dashed lines) at eight sites in JJA 2021. The error bars denote the standard deviation of MAX-DOAS and POMINO-GEMS NO$_2$ at each hour, respectively. Diurnal correlation and all-hour-mean NMB of POMINO-GEMS against MAX-DOAS data are shown. The number of valid days for each hour is also presented. The black squares with an error bar represent the mean value and standard deviation of MAX-DOAS tropospheric NO$_2$ VCDs matched with POMINO-TROPOMI v1.2.2 (blue squares), OMNO2 v4 (orange squares) and GOME-2 GDP 4.8 (green squares), respectively.

As we use TROPOMI total NO$_2$ SCDs to correct those of GEMS, this may influence the NO$_2$ diurnal

variation of original GEMS observations. Thus we also compare MAX-DOAS data with re-calculated

POMINO-GEMS tropospheric NO$_2$ VCDs without correction in total SCDs (red dashed lines in Figure

9). Compared to our default POMINO-GEMS data (with correction), excluding the correction leads to

lower diurnal correlation coefficients at Xuzhou, Hefei, Fudan University, Nanhui and Dianshan Lake,

23

574   but higher correlation coefficients at Xianghe, Chongming and Fukue. Excluding the correction increases

575   the NMB at three sites but decreases the NMB at five sites. We conclude that at these eight sites (in the

576   eastern areas), no significant influence on the diurnal variation of POMINO-GEMS tropospheric NO_2

577   VCDs is brought in through TROPOMI-based correction for total NO_2 SCDs.

578   Figure 10 compares the diurnal variations between POMINO-GEMS and mobile-car MAX-DOAS

579   tropospheric NO_2 VCD data in the Three Rivers' Source region on the Tibetan Plateau. Results of

580   POMINO-GEMS with and without total SCD correction are shown in the red solid and dashed lines,

581   respectively. Mobile-car MAX-DOAS data show an evident decrease of tropospheric NO_2 VCDs from

582   the morning to noon with little change thereafter. Such NO_2 diurnal patterns reflect the spatial and

583   temporal variations of tropospheric NO_2 along the driving route. The high NO_2 values with large standard

584   deviation at 09:00 BJT is due to enhanced pollution and variability in the morning when the car is in or

585   near the Xining city. The NO_2 diurnal variations of POMINO-GEMS with correction correlate well with

586   those of mobile-car MAX-DOAS data (R = 0.81). In contrast, POMINO-GEMS without total SCD

587   correction exhibits much poorer correlation with mobile-car MAX-DOAS data, due to the erroneous

588   increase in the afternoon.

589   Overall, the validation results with independent ground-based and mobile-car MAX-DOAS

590   measurements provide confidence on the general characteristics of POMINO-GEMS NO_2 diurnal

591   variations.

592

3.4 Validation with surface NO$_2$ concentration measurements from MEE

The scatterplot in Figure 11a compares surface NO$_2$ concentrations derived from POMINO-GEMS with MEE measurements at all hours. POMINO-GEMS derived surface NO$_2$ concentrations show good agreement with MEE measurements in terms of spatiotemporal correlation ($R = 0.78$) and bias (NMB = −26.3%), but are higher than those of MEE at some high-value situations, which mainly occur over the YRD region (Figure S14). These differences reflect errors in POMINO-GEMS NO$_2$ VCDs, in the conversion from tropospheric VCDs to surface concentrations, and in MEE data (due to potential contamination by nitric acid and organic nitrates (Liu et al., 2018a)).
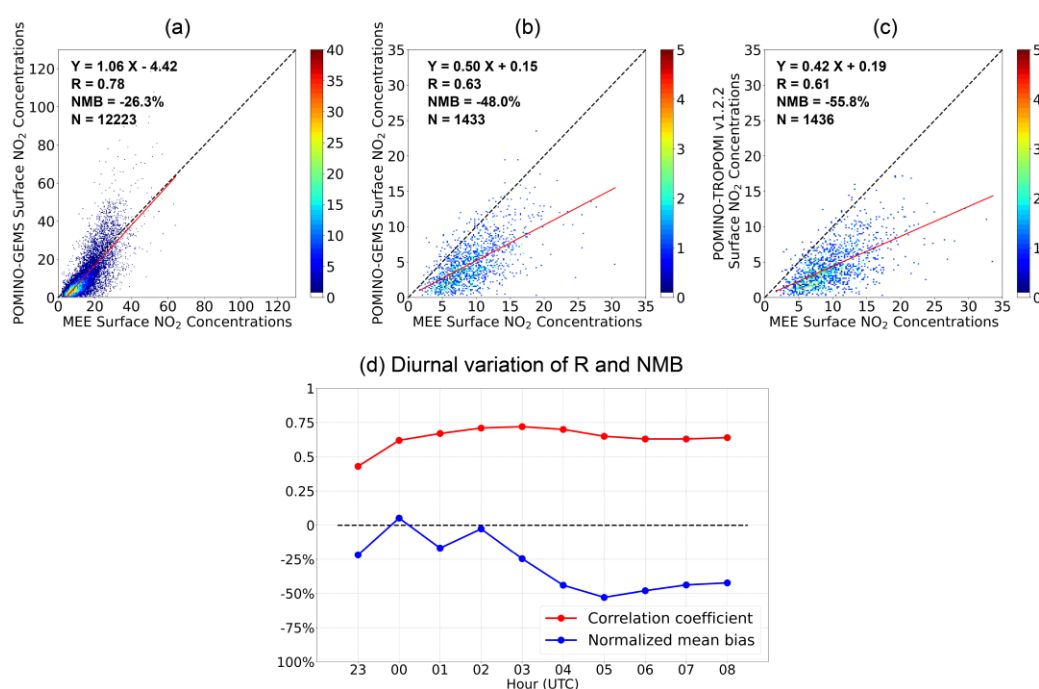
Figure 11. Evaluation of satellite-derived surface NO$_2$ concentrations (µg m^{-3}) using MEE measurements in JJA 2021. (a) Scatterplot for MEE and POMINO-GEMS at all GEMS observation hours averaged over all days in JJA 2021. (b) Scatterplot for MEE and POMINO-GEMS at 13:45 – 14:15 LST. (c) Scatterplot for MEE and POMINO-TROPOMI v1.2.2. The color bar represents the data density. (d) Diurnal variations of spatiotemporal correlation coefficients and NMBs of POMINO-GEMS derived surface NO$_2$ concentrations relative to MEE measurements.

25

616   Figure 11b-c show validation results for satellite-derived surface NO_2 concentrations with MEE

617   measurements at the overpass time of TROPOMI (i.e., early afternoon). Here, each data pair denotes a

618   MEE site. POMINO-GEMS results at 13:45 – 14:15 LST are used to match the overpass time of

619   TROPOMI data. Overall, both satellite-based datasets show good spatial correlation with MEE

620   measurements (R = 0.63 and 0.61). POMINO-GEMS exhibits higher linear regression slope (0.50) with

621   smaller NMB (−48.0%). The values of satellite data are lower than those from MEE, especially in the

622   afternoon (Figure 11d). This is in part because of the aforementioned contamination issues in MEE data,

623   which becomes severer in the afternoon as the air gets more aged throughout the daytime.

624   Figure 12a examines the diurnal variation of surface NO_2 concentrations averaged over JJA 2021 at

625   all sites. The MEE data show a smooth and monotonic decline from the early morning to the early

626   afternoon, with a slight increase beginning at 15:00 LST. This diurnal pattern differs from those seen in

627   ground-based MAX-DOAS VCD data (Figure 9), due to the difference in sampling size between MEE

628   and MAX-DOAS, the diurnal variation of NO_2 vertical distribution that affects the relationship between

629   surface and columnar NO_2, as well as the insensitivity of NO_2 columns to changes in PBL heights.

630   POMINO-GEMS derived surface NO_2 concentrations show similar diurnal variations to those of MEE

631   (R = 0.97), although with a peak at 10:00 LST and a gradual increase beginning at 14:00 LST. The

632   discrepancies between POMINO-GEMS and MEE surface NO_2 concentrations at different hours are

633   likely caused by the assumed constant correction factor of 2 to account for the vertical gradient of NO_2

634   from the height of ground instrument to the center of the first model layer (Section 2.2). In the morning

635   when the PBL is low, most NO_2 molecules are near the ground and the vertical gradient of NO_2 over

636   polluted regions is the largest in the daytime, so the factor of 2 may lead to underestimation of derived

637   surface NO_2 concentrations. In contrast, in the afternoon, the PBL mixing is much stronger and the

638   vertical gradient of NO_2 is much smaller, thus the factor of 2 may lead to overestimated surface NO_2

639   concentrations. Note that the consistency between POMINO-GEMS and MEE data does not depend on

640   the total SCD correction (Table S4).

641   To quantify the influences of the diurnal variation of hourly column-to-surface ratio from GEOS-

642   Chem simulations, we compare the MEE measurements with POMINO-GEMS derived surface NO_2

643   concentrations using daily column-to-surface ratio (Figure S15). As expected, POMINO-GEMS derived

644   NO_2 concentrations show a similar diurnal variation as the tropospheric NO_2 VCDs do, with two peaks

in the mid-morning and afternoon, and a minimum at noon. The temporal correlation coefficient with

MEE is only about 0.23. Thus it is more reasonable to use hourly ratio for comparison with MEE

measurements, as done in our study.

To further test the reliability of our VCD-to-surface-concentration conversion method (Eq. (9)), we

apply the same method to MAX-DOAS NO_2 VCDs and compare the resulting surface NO_2

concentrations with MEE data. As shown in Figure S16, the diurnal variation of MAX-DOAS derived

surface NO_2 concentrations correlates well with that of MEE measurements ($R = 0.96$), in support of our

conversion method.
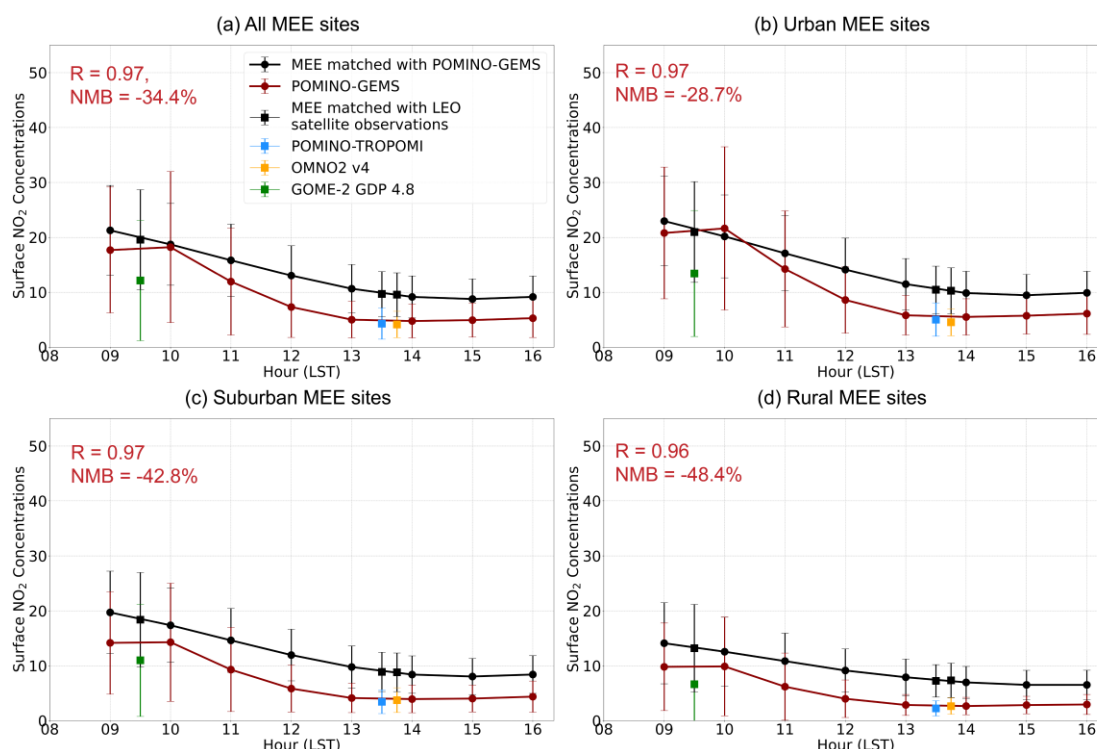
Figure 12. Diurnal variation of hourly surface NO_2 concentrations (μg m^{-3}) of MEE (back lines) and
POMINO-GEMS (red lines) in JJA 2021. (a) At all MEE sites, (b) at urban sites, (c) at suburban sites and
(d) at rural sites. The error bars denote the standard deviation of MEE and POMINO-GEMS derived
surface NO_2 concentrations at each hour in JJA 2021, respectively. Diurnal correlation and mean NMB of
POMINO-GEMS relative to MEE are also listed. The black squares with an error bar represent the mean
value and standard deviation of MEE data matched with POMINO-TROPOMI v1.2.2 (blue squares),
OMNO2 v4 (orange squares) and GOME-2 GDP 4.8 (green squares), respectively.

Figure 12b-d show the comparison of NO_2 diurnal variations for different groups of MEE sites. The

diurnal variations of POMINO-GEMS derived surface NO_2 concentrations show similar characteristics

over urban, suburban and rural regions, and all correlate well with those of MEE data. Meanwhile,

surface NO_2 concentrations derived from LEO satellite observations also agree well with those of

27

665 POMINO-GEMS, except that POMINO-GEMS derived surface NO_2 concentrations are higher than

666 those of GOME-2 GDP 4.8 by about 40% – 60%. We conclude that validation with extensive MEE

667 measurements presents promising performance of POMINO-GEMS retrievals, especially the great

668 agreement of POMINO-GEMS NO_2 diurnal variation with MEE data over urban, suburban and rural

669 regions.

670 **3.5 Error estimates for POMINO-GEMS tropospheric NO_2 VCDs**

671 Total retrieval errors for POMINO-GEMS tropospheric NO_2 VCDs are derived from the

672 calculations of total SCDs, stratospheric SCDs, and tropospheric AMFs. Spatial and temporal averaging

673 across GEMS pixels can greatly reduce the random errors, but will not affect the systematic errors. Here,

674 we provide a preliminary estimate of POMINO-GEMS errors for the summertime retrieval discussed

675 above.

676 As described in Section 2, we calculate hourly total SCDs based on the original GEMS SCD data

677 and daily TROPOMI-guided corrections. According to the GEMS ATBD of NO_2 retrieval algorithm, the

678 SCD errors from the DOAS method are < 5.65% at high-NO_2 conditions (NO_2 VCD > 1×10^{15} molec.

679 cm^{-2}) (Lee et al., 2020). The NO_2 SCD errors of TROPOMI are reported to be $0.5 – 0.6 \times 10^{15}$ molec.

680 cm^{-2} (10% in a relative sense) (Van Geffen et al., 2022a). Given the assumption we made in adjusting

681 GEMS total SCDs to match TROPOMI values, we tentatively estimate the error in our corrected total

682 SCD data to be $0.5 – 0.7 \times 10^{15}$ molec. cm^{-2} (10% in a relative sense) for most regions and 0.9×10^{15}

683 molec. cm^{-2} (20% – 30%) at the edge of the northwestern GEMS FOV.

684 In constructing the stratospheric NO_2 SCDs, the stratospheric VCDs are taken from TROPOMI PAL

685 v2.3.1, scaled based on GEOS-CF v1 stratospheric NO_2 to account for diurnal variation, and then applied

686 with geometric AMFs. We assign a constant error of 0.2×10^{15} molec. cm^{-2} (5% – 10%) to our hourly

687 stratospheric SCDs, the same as the value for TROPOMI (Van Geffen et al., 2022a). Few studies have

688 assessed the accuracy of stratospheric NO_2 and its diurnal variation from GEOS-CF data (Knowland et

689 al., 2022b), but our comparison between GEOS-CF and TROPOMI shows great consistency (Section

690 2.1.5). As most of the errors in total SCDs are absorbed in the stratosphere-troposphere separation step

691 (Van Geffen et al., 2015), the errors in tropospheric SCDs should be 10% – 30% depending on different

692 cases, with higher relative biases in cleaner situations.

693 Tropospheric AMF calculations are the dominant error source for retrieved tropospheric NO_2 VCDs

over polluted regions. According to Liu et al. (2020), the AMF errors caused by uncertainty in surface reflectance are about 10%, and errors induced by uncertainties in aerosol parameters are about 10% in clean regions and 20% for heavily polluted situations. We further assume that the O_2-O_2 cloud retrieval algorithm introduces another error at the 10% level to the NO_2 AMFs. The uncertainty in a priori NO_2 vertical profiles is estimated to cause an AMF error by 10% (Liu et al., 2020). Yang et al. (2023) suggested that the NO_2 profiles from GEOS-Chem (version 13.3.4) might contain incorrect timing of PBL mixing growth in the morning and thus introduce a relative root-mean-square error of 7.6% and NMB of 2.7% in AMF; however, this error could be greatly dampened by averaging over a long time period. The free tropospheric NO_2 bias in GEOS-Chem NO_2 profiles might also contribute to the retrieval errors especially over remote regions. Adding these errors in quadrature leads to the overall AMF errors for POMINO-GEMS at 20% – 40%.

The overall uncertainty in POMINO-GEMS tropospheric NO_2 VCDs is estimated by adding in quadrature the errors in tropospheric NO_2 SCDs and AMFs, when these errors are expressed in the relative sense. For remote regions with low tropospheric NO_2 abundances, the overall retrieval uncertainties can reach 30% – 50% and are dominated by errors in tropospheric SCDs. For regions with abundant tropospheric NO_2, the uncertainties of retrieved tropospheric VCDs are dominated by the AMF errors and are estimated to be about 20% – 30%.

As shown in Figure 8d and Figure 11d, the maximum negative NMB of POMINO-GEMS tropospheric NO_2 VCDs relative to ground-based MAX-DOAS data is about 20% in the mid-morning, and the NMB of POMINO-GEMS derived surface NO_2 concentrations to MEE measurements is −30% on average. Thus our estimated error magnitude is supported by the independent ground-based MAX-DOAS and MEE data.

4. Conclusions

The GEMS instrument provides an unprecedented opportunity for air quality monitoring at a high spatiotemporal resolution. Our POMINO-GEMS algorithm retrieves tropospheric NO_2 VCDs as a research product. The algorithm first calculates hourly tropospheric NO_2 SCDs through fusion of total NO_2 SCDs from the GEMS v1.0 L2 NO_2 product, total and stratospheric NO_2 columns from the TROPOMI PAL v2.3.1 L2 NO_2 product, and stratospheric NO_2 diurnal variations from the GEOS-CF v1 dataset. The fusion approach reduces the high bias in total SCDs and removes the stripe-like patterns in

29

723 the official GEMS v1.0 product. Our algorithm then calculates tropospheric NO_2 AMFs to convert SCDs

724 to VCDs. A preliminary estimate of retrieval errors is also given.

725 Our initial POMINO-GEMS data for JJA 2021 shows high values of tropospheric NO_2 VCDs with

726 clear hotspots ($> 10 \times 10^{15}$ molec. cm^{-2}) over regions where anthropogenic emissions of NO_x are abundant.

727 The spatial gradients of tropospheric NO_2 VCDs from urban centers to surrounding areas are substantial

728 in the morning due to traffic emissions, but the gradients are much reduced at noon and in the afternoon.

729 A gradual increase of tropospheric NO_2 VCDs from the morning to noon is observed over clean regions

730 of western China, likely as a result of enhanced biogenic emissions. Over high NO_2 regions where

731 anthropogenic activities dominate the NO_x emissions, NO_2 columns increase until a peak at $09:00 - 10:00$

732 LST, decrease to the minimum at noon and then increase in the afternoon again. Such characteristics of

733 NO_2 diurnal variations are associated with the changes in natural and anthropogenic NO_x emissions,

734 photochemistry and atmospheric transport.

735 POMINO-GEMS tropospheric NO_2 VCDs agree well with POMINO-TROPOMI v1.2.2 in terms of

736 spatial correlation (0.98) and NMB (4.9%). POMINO-GEMS data are also consistent with the OMNO2

737 v4 tropospheric NO_2 VCD product in the early afternoon and GOME-2 GDP 4.8 tropospheric NO_2 VCD

738 product in the morning, with R of 0.87 and 0.83, and NMB of -16.8% and -1.5%, respectively.

739 POMINO-GEMS tropospheric NO_2 VCDs are comparable with ground-based MAX-DOAS

740 measurements at nine ground-based sites with a small NMB (-11.1%), although the correlation is modest

741 ($R = 0.66$). Both the bias and correlation values are smaller than POMINO-TROPOMI v1.2.2 (NMB =

742 -18.1%, $R = 0.83$). More importantly, POMINO-GEMS well captures the diurnal variation of MAX-

743 DOAS NO_2 VCDs at Xuzhou ($R = 0.82$), Hefei ($R = 0.96$), Fudan University ($R = 0.84$), Nanhui ($R =$

744 0.79), Xianghe ($R = 0.94$) and Dianshan Lake ($R = 0.60$) sites, although the correlations are relatively

745 poor at Chongming and Fukue sites. Comparison with mobile-car MAX-DOAS measurements in the

746 Three Rivers' Source region on the Tibetan Plateau also shows good correlation in NO_2 diurnal variation

747 ($R = 0.81$).

748 We also compare surface NO_2 concentrations derived from tropospheric NO_2 VCDs in POMINO-

749 GEMS and POMINO-TROPOMI v1.2.2 against MEE data, taking advantage of the large number of

750 MEE sites. POMINO-GEMS derived surface NO_2 concentration data exhibit a small NMB (-26.3%).

751 For these sites at TROPOMI overpass times, POMINO-GEMS derived surface NO_2 concentrations show

a smaller magnitude of NMB (−48.0%) than POMINO-TROPOMI v1.2.2 (−55.8%). Excellent

agreement in diurnal variation between POMINO-GEMS derived and MEE NO_2 is exhibited over all (R

= 0.97), urban (R = 0.97), suburban (R = 0.97) and rural (R = 0.96) sites.

Overall, our comprehensive validation process highlights the good performance of POMINO-GEMS tropospheric NO_2 VCD product, both in magnitude and spatiotemporal variation. However, there are still several limitations in our study. To address the systematic overestimation and stripes problems in the original GEMS data, we correct GEMS total NO_2 SCDs by using TROPOMI data as a temporary solution. For example, we implement a simple geometric correction to combine GEMS and TROPOMI total NO_2 SCDs, but their differences in scattering geometry are only partly accounted for. Thus this correction works well in most regions, but may introduce SCD uncertainties up to 0.9×10^{15} molec. cm^{-2} (20% – 30%) at the edge of the northwestern GEMS FOV. Currently, the Environmental Satellite Center of South Korea is updating the NO_2 SCD data to v2.0. We will update our POMINO-GEMS algorithm accordingly, once the updated official NO_2 product becomes available to provide necessary inputs for our research product. In addition, in the conversion from NO_2 VCDs to surface concentrations, we use a constant correction factor of 2 to account for the strong NO_2 vertical gradient near the surface. This simple treatment does not account for the diurnal variation of the correction factor, and thus may introduce errors in the derived surface NO_2 concentrations. Nevertheless, the current POMINO-GEMS data serve as our initial attempt to derive the diurnal variations of tropospheric NO_2 at a high spatiotemporal resolution from GEMS, and they are expected to offer a useful source of information for various applications such as air quality analysis and emission constraint.

Data availability. The POMINO-GEMS NO_2 data will be freely available soon at the ACM group product website (http://www.pku-atmos-acm.org/acmProduct.php/). The TROPOMI PAL v2.3.1 L2 product can be downloaded from https://data-portal.s5p-pal.com. The OMNO2 v4 L2 product can be downloaded from https://aura.gesdisc.eosdis.nasa.gov/data/Aura_OMI_Level2/OMNO2.003/. The GOME-2 GDP 4.8 L2 product can be downloaded from http://acsaf.org/ after registration. The GEOS-CF v1.0 dataset can be downloaded from https://gmao.gsfc.nasa.gov/weather_prediction/GEOS-CF/data_access/. The MEE surface NO_2 measurements can be downloaded from https://quotsoft.net/air/. The ground-based and mobile-car MAX-DOAS measurements can be provided upon requests to the

781　corresponding owners.

782

795

796　**References**

797　　Beirle, S., Boersma, K. F., Platt, U., Lawrence, M. G., and Wagner, T.: Megacity Emissions and

798　Lifetimes of Nitrogen Oxides Probed from Space, Science, 333, 1737-1739, 10.1126/science.1207824,

799　2011.

800　　Biswas, M. S. and Mahajan, A. S.: Year-long Concurrent MAX-DOAS Observations of Nitrogen

801　Dioxide and Formaldehyde at Pune: Understanding Diurnal and Seasonal Variation Drivers, Aerosol and

802　Air Quality Research, 21, 200524, 10.4209/aaqr.200524, 2021.

803　　Boersma, K. F., Eskes, H. J., and Brinksma, E. J.: Error analysis for tropospheric NO_2 retrieval from

804　space, Journal of Geophysical Research: Atmospheres, 109, n/a-n/a, 10.1029/2003jd003962, 2004.

805　　Boersma, K. F., Jacob, D. J., Eskes, H. J., Pinder, R. W., Wang, J., and Van Der A, R. J.:

806　Intercomparison of SCIAMACHY and OMI tropospheric NO_2 columns: Observing the

807　diurnal evolution of chemistry and emissions from space, Journal of Geophysical Research, 113,

808　10.1029/2007jd008816, 2008.

809　　Boersma, K. F., Jacob, D. J., Trainic, M., Rudich, Y., Desmedt, I., Dirksen, R., and Eskes, H. J.:

Validation of urban NO_2 concentrations and their diurnal and seasonal variations observed from the SCIAMACHY and OMI sensors using in situ surface measurements in Israeli cities, Atmospheric Chemistry and Physics, 9, 3867-3879, 10.5194/acp-9-3867-2009, 2009.

Boersma, K. F., Eskes, H. J., Dirksen, R. J., van der A, R. J., Veefkind, J. P., Stammes, P., Huijnen, V., Kleipool, Q. L., Sneep, M., Claas, J., Leitão, J., Richter, A., Zhou, Y., and Brunner, D.: An improved tropospheric NO2 column retrieval algorithm for the Ozone Monitoring Instrument, Atmospheric Measurement Techniques, 4, 1905-1928, 10.5194/amt-4-1905-2011, 2011.

Burrows, J. P.: The Global Ozone Monitoring Experiment (GOME) : Mission concept and first scientific results, Journal of Atmospheric Sciences, 56, 2340-2352, 1999.

Callies, J., Corpaccioli, E., Eisinger, M., Hahne, A., and Lefebvre, A.: GOME-2 – Metop's Second-Generation Sensor for Operational Ozone Monitoring,

Chen, L., Lin, J., Martin, R., Du, M., Weng, H., Kong, H., Ni, R., Meng, J., Zhang, Y., Zhang, L., and van Donkelaar, A.: Inequality in historical transboundary anthropogenic PM2.5 health impacts, Science Bulletin, https://doi.org/10.1016/j.scib.2021.11.007, 2021.

Chen, L., Lin, J., Ni, R., Kong, H., Du, M., Yan, Y., Liu, M., Wang, J., Weng, H., Zhao, Y., Li, C., and Martin, R. V.: Historical transboundary ozone health impact linked to affluence, Environmental Research Letters, 17, 104014, 10.1088/1748-9326/ac9009, 2022.

Cheng, S., Cheng, X., Ma, J., Xu, X., Zhang, W., Lv, J., Bai, G., Chen, B., Ma, S., Ziegler, S., Donner, S., and Wagner, T.: Mobile MAX-DOAS observations of tropospheric NO2 and HCHO during summer over the Three Rivers' Source region in China, Atmos. Chem. Phys., 23, 3655-3677, 10.5194/acp-23-3655-2023, 2023.

Cooper, M. J., Martin, R. V., Hammer, M. S., Levelt, P. F., Veefkind, P., Lamsal, L. N., Krotkov, N. A., Brook, J. R., and Mclinden, C. A.: Global fine-scale changes in ambient NO2 during COVID-19 lockdowns, Nature, 601, 380-387, 10.1038/s41586-021-04229-0, 2022.

Crutzen, P. J.: The influence of nitrogen oxides on the atmospheric ozone content, Quarterly Journal of the Royal Meteorological Society, 96, 320-325, 10.1002/qj.49709640815, 1970.

Cui, Y., Lin, J., Song, C., Liu, M., Yan, Y., Xu, Y., and Huang, B.: Rapid growth in nitrogen dioxide pollution over Western China, 2005–2013, Atmos. Chem. Phys., 16, 6207-6221, 10.5194/acp-16-6207-2016, 2016.

839   Dirksen, R. J., Boersma, K. F., Eskes, H. J., Ionov, D. V., Bucsela, E. J., Levelt, P. F., and Kelder, H.

840   M.: Evaluation of stratospheric NO2 retrieved from the Ozone Monitoring Instrument: Intercomparison,

841   diurnal cycle, and trending, Journal of Geophysical Research, 116, 10.1029/2010jd014943, 2011.

842   Eastham, S. D., Weisenstein, D. K., and Barrett, S. R. H.: Development and evaluation of the unified

843   tropospheric–stratospheric chemistry extension (UCX) for the global chemistry-transport model GEOS-

844   Chem, Atmospheric Environment, 89, 52-63, https://doi.org/10.1016/j.atmosenv.2014.02.001, 2014.

845   Eskes, H., Van Geffen, J., Sneep, M., Veefkind, P., Niemeier, S., and Zehner, C.: S5P Nitrogen

846   Dioxide v02.03.01 intermediate reproecessing on the S5P-PAL system: Readme file, 2021.

847   Ghude, S. D., Karumuri, R. K., Jena, C., Kulkarni, R., Pfister, G. G., Sajjan, V. S., Pithani, P.,

848   Debnath, S., Kumar, R., Upendra, B., Kulkarni, S. H., Lal, D. M., Vander A, R. J., and Mahajan, A. S.:

849   What is driving the diurnal variation in tropospheric NO2 columns over a cluster of high emission

850   thermal power plants in India?, Atmospheric Environment: X, 5, 100058,

851   https://doi.org/10.1016/j.aeaoa.2019.100058, 2020.

852   Grubbs, F. E.: Sample Criteria for Testing Outlying Observations, The Annals of Mathematical

853   Statistics, 21, 27-58, 10.1214/aoms/1177729885, 1950.

854   Gu, D., Wang, Y., Smeltzer, C., and Boersma, K. F.: Anthropogenic emissions of NOx over China:

855   Reconciling the difference of inverse modeling results using GOME-2 and OMI measurements, Journal

856   of Geophysical Research: Atmospheres, 119, 7732-7740, 10.1002/2014jd021644, 2014.

857   Hendrick, F., Müller, J.-F., Clémer, K., Wang, P., De Mazière, M., Fayt, C., Gielen, C., Hermans, C.,

858   Ma, J. Z., Pinardi, G., Stavrakou, T., Vlemmix, T., and Van Roozendael, M.: Four years of ground-based

859   MAX-DOAS observations of HONO and NO$_2$ in the Beijing area, Atmospheric Chemistry

860   and Physics, 14, 765-781, 10.5194/acp-14-765-2014, 2014.

861   Herman, J., Abuhassan, N., Kim, J., Kim, J., Dubey, M., Raponi, M., and Tzortziou, M.:

862   Underestimation of column NO2 amounts from the OMI satellite compared to diurnally varying ground-

863   based retrievals from multiple PANDORA spectrometer instruments, Atmos. Meas. Tech., 12, 5593-5612,

864   10.5194/amt-12-5593-2019, 2019.

865   Hoek, G., Krishnan, R. M., Beelen, R., Peters, A., Ostro, B., Brunekreef, B., and Kaufman, J. D.:

866   Long-term air pollution exposure and cardio- respiratory mortality: a review, Environmental Health, 12,

867   43, 10.1186/1476-069X-12-43, 2013.

Jing, B., Wu, L., Mao, H., Gong, S., He, J., Zou, C., Song, G., Li, X., and Wu, Z.: Development of a vehicle emission inventory with high temporal–spatial   resolution based on NRT traffic data and its impact on air pollution in   Beijing – Part 1: Development and evaluation of vehicle emission inventory, Atmospheric Chemistry and Physics, 16, 3161-3170, 10.5194/acp-16-3161-2016, 2016.

Kanaya, Y., Irie, H., Takashima, H., Iwabuchi, H., Akimoto, H., Sudo, K., Gu, M., Chong, J., Kim, Y. J., Lee, H., Li, A., Si, F., Xu, J., Xie, P.-H., Liu, W.-Q., Dzhola, A., Postylyakov, O., Ivanov, V., Grechko, E., Terpugova, S., and Panchenko, M.: Long-term MAX-DOAS network observations of NO_2 in Russia and Asia (MADRAS) during the period 2007–2012: instrumentation, elucidation of climatology, and comparisons with OMI satellite observations and global model si, Atmospheric Chemistry and Physics, 14, 7909-7927, 10.5194/acp-14-7909-2014, 2014.

Keller, C. A., Knowland, K. E., Duncan, B. N., Liu, J., Anderson, D. C., Das, S., Lucchesi, R. A., Lundgren, E. W., Nicely, J. M., Nielsen, E., Ott, L. E., Saunders, E., Strode, S. A., Wales, P. A., Jacob, D. J., and Pawson, S.: Description of the NASA GEOS Composition Forecast Modeling System GEOS-CF v1.0, Journal of Advances in Modeling Earth Systems, 13, 10.1029/2020ms002413, 2021.

Kim, J., Jeong, U., Ahn, M.-H., Kim, J. H., Park, R. J., Lee, H., Song, C. H., Choi, Y.-S., Lee, K.-H., Yoo, J.-M., Jeong, M.-J., Park, S. K., Lee, K.-M., Song, C.-K., Kim, S.-W., Kim, Y. J., Kim, S.-W., Kim, M., Go, S., Liu, X., Chance, K., Chan Miller, C., Al-Saadi, J., Veihelmann, B., Bhartia, P. K., Torres, O., Abad, G. G., Haffner, D. P., Ko, D. H., Lee, S. H., Woo, J.-H., Chong, H., Park, S. S., Nicks, D., Choi, W. J., Moon, K.-J., Cho, A., Yoon, J., Kim, S.-K., Hong, H., Lee, K., Lee, H., Lee, S., Choi, M., Veefkind, P., Levelt, P. F., Edwards, D. P., Kang, M., Eo, M., Bak, J., Baek, K., Kwon, H.-A., Yang, J., Park, J., Han, K. M., Kim, B.-R., Shin, H.-W., Choi, H., Lee, E., Chong, J., Cha, Y., Koo, J.-H., Irie, H., Hayashida, S., Kasai, Y., Kanaya, Y., Liu, C., Lin, J., Crawford, J. H., Carmichael, G. R., Newchurch, M. J., Lefer, B. L., Herman, J. R., Swap, R. J., Lau, A. K. H., Kurosu, T. P., Jaross, G., Ahlers, B., Dobber, M., Mcelroy, C. T., and Choi, Y.: New Era of Air Quality Monitoring from Space: Geostationary Environment Monitoring Spectrometer (GEMS), Bulletin of the American Meteorological Society, 101, E1-E22, 10.1175/bams-d-18-0013.1, 2020.

Kim, S., Kim, D., Hong, H., Chang, L. S., Lee, H., Kim, D. R., Kim, D., Yu, J. A., Lee, D., Jeong, U., Song, C. K., Kim, S. W., Park, S. S., Kim, J., Hanisco, T. F., Park, J., Choi, W., and Lee, K.: First-time comparison between NO2 vertical columns from GEMS and Pandora measurements, Atmos. Meas.

897 Tech. Discuss., 2023, 1-22, 10.5194/amt-2023-11, 2023.

898 Knowland, K. E., Keller, C. A., and Lucchesi, R. A.: File Specification for GEOS-CF Products,

899 2022a.

900 Knowland, K. E., Keller, C. A., Wales, P. A., Wargan, K., Coy, L., Johnson, M. S., Liu, J., Lucchesi,

901 R. A., Eastham, S. D., Fleming, E., Liang, Q., Leblanc, T., Livesey, N. J., Walker, K. A., Ott, L. E., and

902 Pawson, S.: NASA GEOS Composition Forecast Modeling System GEOS-CF v1.0: Stratospheric

903 Composition, Journal of Advances in Modeling Earth Systems, 14, e2021MS002852,

904 https://doi.org/10.1029/2021MS002852, 2022b.

905 Kong, H., Lin, J., Chen, L., Zhang, Y., Yan, Y., Liu, M., Ni, R., Liu, Z., and Weng, H.: Considerable

906 Unaccounted Local Sources of NOx Emissions in China Revealed from Satellite, Environmental Science

907 & Technology, 56, 7131-7142, 10.1021/acs.est.1c07723, 2022a.

908 Kong, H., Lin, J., Zhang, Y., Li, C., Xu, C., Shen, L., Liu, X., Yang, K., Su, H., and Xu, W.:

909 Unexpected high NOX emissions from lakes on Tibetan Plateau under rapid warming, 10.21203/rs.3.rs-

910 1980236/v1, 2022b.

911 Kong, H., Lin, J., Zhang, Y., Li, C., Xu, C., Shen, L., Liu, X., Yang, K., Su, H., and Xu, W.: High

912 natural nitric oxide emissions from lakes on Tibetan Plateau under rapid warming, Nature Geoscience,

913 16, 474-477, 10.1038/s41561-023-01200-8, 2023.

914 Krotkov, N., Lamsal, L. N., Marchenko, S., and Swartz, W. H.: OMNO2 README Document Data

915 Product Version 4.0, 2019.

916 Krotkov, N. A., McLinden, C. A., Li, C., Lamsal, L. N., Celarier, E. A., Marchenko, S. V., Swartz,

917 W. H., Bucsela, E. J., Joiner, J., Duncan, B. N., Boersma, K. F., Veefkind, J. P., Levelt, P. F., Fioletov, V.

918 E., Dickerson, R. R., He, H., Lu, Z., and Streets, D. G.: Aura OMI observations of regional SO2 and NO2

919 pollution changes from 2005 to 2015, Atmos. Chem. Phys., 16, 4605-4629, 10.5194/acp-16-4605-2016,

920 2016.

921 Lee, H., Park, J., and Hong, H.: Geostationary Environment Monitoring Spectrometer (GEMS)

922 Algorithm Theoretical Basis Document NO2 Retrieval Algorithm, 2020.

923 Lee, Y., Ahn, M. H., Kang, M., and Eo, M.: Spectral replacement using machine learning methods

924 for continuous mapping of the Geostationary Environment Monitoring Spectrometer (GEMS), Atmos.

925 Meas. Tech., 16, 153-168, 10.5194/amt-16-153-2023, 2023.

926   Levelt, P. F., Van Den Oord, G. H. J., Dobber, M. R., Malkki, A., Visser, H., Vries, J. D., Stammes,

927 P., Lundell, J. O. V., and Saari, H.: The ozone monitoring instrument, IEEE Transactions on Geoscience

928 and Remote Sensing, 44, 1093-1101, 10.1109/tgrs.2006.872333, 2006.

929   Li, J., Wang, Y., Zhang, R., Smeltzer, C., Weinheimer, A., Herman, J., Boersma, K. F., Celarier, E.

930 A., Long, R. W., Szykman, J. J., Delgado, R., Thompson, A. M., Knepp, T. N., Lamsal, L. N., Janz, S. J.,

931 Kowalewski, M. G., Liu, X., and Nowlan, C. R.: Comprehensive evaluations of diurnal NO2

932 measurements during DISCOVER-AQ 2011: effects of resolution-dependent representation of NOx

933 emissions, Atmos. Chem. Phys., 21, 11133-11160, 10.5194/acp-21-11133-2021, 2021a.

934   Li, K.-F., Khoury, R., Pongetti, T. J., Sander, S. P., Mills, F. P., and Yung, Y. L.: Diurnal variability

935 of stratospheric column NO_2 measured using direct solar and lunar spectra over Table

936 Mountain, California (34.38° N), Atmospheric Measurement Techniques, 14, 7495-7510, 10.5194/amt-

937 14-7495-2021, 2021b.

938   Lin, J. T. and McElroy, M. B.: Detection from space of a reduction in anthropogenic emissions of

939 nitrogen oxides during the Chinese economic downturn, Atmos. Chem. Phys., 11, 8171-8188,

940 10.5194/acp-11-8171-2011, 2011.

941   Lin, J. T., Liu, M. Y., Xin, J. Y., Boersma, K. F., Spurr, R., Martin, R., and Zhang, Q.: Influence of

942 aerosols and surface reflectance on satellite NO2 retrieval: seasonal and spatial characteristics and

943 implications for NOx emission constraints, Atmospheric Chemistry and Physics, 15, 11217-11241,

944 10.5194/acp-15-11217-2015, 2015.

945   Lin, J. T., Martin, R. V., Boersma, K. F., Sneep, M., Stammes, P., Spurr, R., Wang, P., Van

946 Roozendael, M., Clémer, K., and Irie, H.: Retrieving tropospheric nitrogen dioxide from the Ozone

947 Monitoring Instrument: effects of aerosols, surface reflectance anisotropy, and vertical profile of nitrogen

948 dioxide, Atmospheric Chemistry and Physics, 14, 1441-1461, 10.5194/acp-14-1441-2014, 2014.

949   Liu, M., Lin, J., Wang, Y., Sun, Y., Zheng, B., Shao, J., Chen, L., Zheng, Y., Chen, J., Fu, T. M., Yan,

950 Y., Zhang, Q., and Wu, Z.: Spatiotemporal variability of NO2 and PM2.5 over Eastern China:

951 observational and model analyses with a novel statistical method, Atmos. Chem. Phys., 18, 12933-12952,

952 10.5194/acp-18-12933-2018, 2018a.

953   Liu, M., Lin, J., Kong, H., Boersma, K. F., Eskes, H., Kanaya, Y., He, Q., Tian, X., Qin, K., Xie, P.,

954 Spurr, R., Ni, R., Yan, Y., Weng, H., and Wang, J.: A new TROPOMI product for tropospheric NO2

955 columns over East Asia with explicit aerosol corrections, Atmos. Meas. Tech., 13, 4247-4259,

956 10.5194/amt-13-4247-2020, 2020.

957 Liu, M., Lin, J., Boersma, K. F., Pinardi, G., Wang, Y., Chimot, J., Wagner, T., Xie, P., Eskes, H.,

958 Van Roozendael, M., Hendrick, F., Wang, P., Wang, T., Yan, Y., Chen, L., and Ni, R.: Improved aerosol

959 correction for OMI tropospheric NO2 retrieval over East Asia: constraint from CALIOP aerosol vertical

960 profile, Atmospheric Measurement Techniques, 12, 1-21, 10.5194/amt-12-1-2019, 2019.

961 Liu, Y.-H., Ma, J.-L., Li, L., Lin, X.-F., Xu, W.-J., and Ding, H.: A high temporal-spatial vehicle

962 emission inventory based on detailed hourly traffic data in a medium-sized city of China, Environmental

963 Pollution, 236, 324-333, https://doi.org/10.1016/j.envpol.2018.01.068, 2018b.

964 Lorente, A., Boersma, K. F., Stammes, P., Tilstra, L. G., and Muller, J. P.: The importance of surface

965 reflectance anisotropy for cloud and NO2 retrievals from GOME-2 and OMI, 2018.

966 Lorente, A., Boersma, K. F., Yu, H., Dorner, S., Hilboll, A., Richter, A., Liu, M., Lamsal, L. N.,

967 Barkley, M. P., and De Smedt, I.: Structural uncertainty in air mass factor calculation for NO2 and HCHO

968 satellite retrievals, Atmospheric Measurement Techniques, 10, 759-782, 2016.

969 Lucht, W., Schaaf, C. B., and Strahler, A. H.: An algorithm for the retrieval of albedo from space

970 using semiempirical BRDF models, IEEE Transactions on Geoscience & Remote Sensing, 38, 977-998,

971 2000.

972 Naiudomthum, S., Winijkul, E., and Sirisubtawee, S.: Near Real-Time Spatial and Temporal

973 Distribution of Traffic Emissions in Bangkok Using Google Maps Application Program Interface,

974 Atmosphere, 13, 1803, 10.3390/atmos13111803, 2022.

975 Palmer, P. I., Jacob, D. J., Chance, K., Martin, R. V., Spurr, R. J. D., Kurosu, T. P., Bey, I., Yantosca,

976 R., Fiore, A., and Li, Q.: Air mass factor formulation for spectroscopic measurements from satellites:

977 Application to formaldehyde retrievals from the Global Ozone Monitoring Experiment, Journal of

978 Geophysical Research: Atmospheres, 106, 14539-14550, 10.1029/2000jd900772, 2001.

979 Richter, A., Burrows, J. P., Nüß, H., Granier, C., and Niemeier, U.: Increase in tropospheric nitrogen

980 dioxide over China observed from space, Nature, 437, 129-132, 10.1038/nature04092, 2005.

981 Shindell, D. T., Faluvegi, G., Koch, D. M., Schmidt, G. A., Unger, N., and Bauer, S. E.: Improved

982 Attribution of Climate Forcing to Emissions, Science, 326, 716-718, 10.1126/science.1174760, 2009.

983 Valks, P.: Algorithm Theoretical Basis Document for GOME-2 Total Column Products of Ozone,

NO2, BrO, SO2, H2O, HCHO, OClO and Cloud Properties (GDP 4.8/4.9), 2019.

Valks, P., Chan, L., Zimmer, W., Hedelt, P., and Slijkhuis, S.: PRODUCT USER MANUAL GOME-2 Total Column Products of Ozone, NO2, BrO, HCHO, SO2, H2O, OClO and Cloud Properties GDP 4.8 for GOME-2 on MetOp-A and -B GDP 4.9 for GOME-2 on MetOp-C, 2019.

van der A, R. J., Mijling, B., Ding, J., Koukouli, M. E., Liu, F., Li, Q., Mao, H., and Theys, N.: Cleaning up the air: effectiveness of air quality policy for SO2 and NOx emissions in China, Atmos. Chem. Phys., 17, 1775-1789, 10.5194/acp-17-1775-2017, 2017.

Van Geffen, J., Eskes, H., Boersma, K. F., and Veefkind, P.: TROPOMI ATBD of the total and tropospheric NO2 data products, 2022a.

Van Geffen, J., Eskes, H., Compernolle, S., Pinardi, G., Verhoelst, T., Lambert, J.-C., Sneep, M., Ter Linden, M., Ludewig, A., Boersma, K. F., and Veefkind, J. P.: Sentinel-5P TROPOMI NO_2 retrieval: impact of version v2.2 improvements and comparisons with OMI and ground-based data, Atmospheric Measurement Techniques, 15, 2037-2060, 10.5194/amt-15-2037-2022, 2022b.

Vasilkov, A., Krotkov, N., Yang, E. S., Lamsal, L., Joiner, J., Castellanos, P., Fasnacht, Z., and Spurr, R.: Explicit and consistent aerosol correction for visible wavelength satellite cloud and nitrogen dioxide retrievals based on optical properties from a global aerosol analysis, Atmos. Meas. Tech., 14, 2857-2871, 10.5194/amt-14-2857-2021, 2021.

Vasilkov, A. P., Qin, W., Krotkov, N. A., Lamsal, L. N., Spurr, R., Haffner, D. P., Joiner, J., Yang, E., and Marchenko, S.: Accounting for the Effects of Surface BRDF on Satellite Cloud and Trace-Gas Retrievals: A New Approach Based on Geometry-Dependent Lambertian-Equivalent Reflectivity Applied to OMI Algorithms, Atmospheric Measurement Techniques, 10, 333-349, 2016.

Veefkind, J. P., Aben, I., McMullan, K., Förster, H., de Vries, J., Otter, G., Claas, J., Eskes, H. J., de Haan, J. F., Kleipool, Q., van Weele, M., Hasekamp, O., Hoogeveen, R., Landgraf, J., Snel, R., Tol, P., Ingmann, P., Voors, R., Kruizinga, B., Vink, R., Visser, H., and Levelt, P. F.: TROPOMI on the ESA Sentinel-5 Precursor: A GMES mission for global observations of the atmospheric composition for climate, air quality and ozone layer applications, Remote Sensing of Environment, 120, 70-83, https://doi.org/10.1016/j.rse.2011.09.027, 2012.

Wei, J., Liu, S., Li, Z., Liu, C., Qin, K., Liu, X., Pinker, R. T., Dickerson, R. R., Lin, J., Boersma,

K. F., Sun, L., Li, R., Xue, W., Cui, Y., Zhang, C., and Wang, J.: Ground-Level NO_2 Surveillance from Space Across China for High Resolution Using Interpretable Spatiotemporally Weighted Artificial Intelligence, Environmental Science & Technology, 56, 9988-9998, 10.1021/acs.est.2c03834, 2022.

Weng, H., Lin, J., Martin, R., Millet, D. B., Jaeglé, L., Ridley, D., Keller, C., Li, C., Du, M., and Meng, J.: Global high-resolution emissions of soil NOx, sea salt aerosols, and biogenic volatile organic compounds, Scientific Data, 7, 148, 10.1038/s41597-020-0488-5, 2020.

Yang, L. H., Jacob, D. J., Colombi, N. K., Zhai, S., Bates, K. H., Shah, V., Beaudry, E., Yantosca, R. M., Lin, H., Brewer, J. F., Chong, H., Travis, K. R., Crawford, J. H., Lamsal, L. N., Koo, J. H., and Kim, J.: Tropospheric NO2 vertical profiles over South Korea and their relation to oxidant chemistry: implications for geostationary satellite retrievals and the observation of NO2 diurnal variation from space, Atmos. Chem. Phys., 23, 2465-2481, 10.5194/acp-23-2465-2023, 2023.

Zhang, Y., Lin, J., Liu, M., Kong, H., Chen, L., Weng, H., and Li, C.: High-resolution Tropospheric NO2 Retrieval over Asia based on OMI POMINO v2.1 and Quantitative comparison with other products, National Remote Sensing Bulletin, 10.11834/jrs.20221413, 2022.

Zhou, Y., Brunner, D., Spurr, R. J. D., Boersma, K. F., Sneep, M., Popp, C., and Buchmann, B.: Accounting for surface reflectance anisotropy in satellite retrievals of tropospheric NO2, Atmospheric Measurement Techniques, 3, 1185-1203, 2010.